

A $(g - 2)_\mu$ Experiment to ± 0.2 ppm Precision

BNL P969

New $(g - 2)_\mu$ Collaboration: R.M. Carey¹, A. Gafarov¹, I. Logashenko¹, K.R. Lynch¹, J.P. Miller¹, B.L. Roberts¹, G. Bunce², W. Meng², W.M. Morse², Y.K. Semertzidis², D. Grigoriev³, B.I. Khazin³, S.I. Redin³, Yuri M. Shatunov³, E. Solodov³, Y. Orlov⁴, P. Debevec⁵, D.W. Hertzog⁵, P. Kammel⁵, R. McNabb⁵, F. Mülhauser⁵, K.L. Giovanetti⁶, K.P. Jungmann⁷, C.J.G. Onderwater⁷, S. Dhamija⁸, T.P. Gorringe⁸, W. Korsch⁸, F.E. Gray⁹, B. Lauss⁹, E.P. Sichtermann⁹, P. Cushman¹⁰, T. Qian¹⁰, P. Shagin¹⁰, S. Dhawan¹¹, and F.J.M. Farley¹¹

¹Department of Physics, Boston University, Boston, MA 02215

²Brookhaven National Laboratory, Upton, NY 11973

³Budker Institute of Nuclear Physics, Novosibirsk, Russia

⁴Newman Laboratory, Cornell University, Ithaca, New York 14853

⁵Department of Physics, University of Illinois, Urbana-Champaign, IL 61801

⁶Department of Physics, James Madison University, Harrisonburg VA 22807

⁷Kernfysisch Versneller Instituut, Rijksuniversiteit,

Groningen, NL 9747 AA Groningen, the Netherlands

⁸Department of Physics, University of Kentucky, Lexington, Kentucky 40506

⁹University of California, Berkeley and Lawrence Berkeley Laboratory, Berkeley, CA 94720

¹⁰Department of Physics, University of Minnesota, Minneapolis, MN 55455

¹¹ Department of Physics, Yale University, New Haven, Connecticut 06520

Fast extracted proton beam to the V-target. 12 or 24 bunches per AGS cycle, 60 TP per cycle, minimum possible AGS cycle time.

Spokespersons: B. Lee Roberts (roberts@bu.edu, 617-353-2187)
David W. Hertzog (hertzog@uiuc.edu, 217-333-3988)

Resident-spokesperson: William M. Morse (morse@bnl.gov, 631-344-3859)

Abstract

The E821 Collaboration measured the muon anomalous magnetic moment a_μ to a precision of 0.54 ppm. It differs from standard model theory by 2.4 standard deviations. We propose to carry out an upgraded effort at the AGS to reach a precision of ± 0.2 ppm, a factor of 2.5 improvement. This step forward will be well matched to anticipated advances in the worldwide effort to determine the standard model theoretical value for a_μ . With the anticipated improved theory value, the future experiment-theory comparison would have an uncertainty of $\approx 4 - 5 \times 10^{-10}$, allowing stringent tests of standard model extensions. The principal feature of the new experiment is a redesigned pion / muon beamline that will deliver a significantly higher muon flux and eliminate the hadronic flash at injection. The higher statistical sample will require a new detector, electronics and data acquisition system and a reduction in the major systematic uncertainties. This proposal outlines a plan to carry out this experiment—at BNL—making optimum use of the considerable investment in the E821 storage ring and associated experimental elements. Because the major changes planned do not require extensive R&D, we can be ready for a commissioning run two years after approval and funding, and ready for a production run approximately one year later. We request a period of “pulse on demand” running using fast extraction to the V-line, followed by 3 weeks of engineering running. A major data collection run of 21 weeks would follow one year after the engineering run.

Contents

I. Executive Summary	5
II. Introduction	6
III. E821 Review	8
IV. The Standard Model Value of the Anomaly	11
A. QED and Weak Contributions	12
B. The Hadronic Contribution	12
C. $a_\mu^{\text{had;LO}}$ from Hadronic τ decay?	15
D. The Hadronic Light-by-light Contribution	17
E. Summary of the Standard Model Value and Comparison with Experiment	17
F. Expected Improvements in the Standard Model Value	18
G. Physics Beyond the Standard Model	20
V. A New $(g - 2)$ Experiment	22
A. Scientific Goal	22
B. Strategy of a new experiment	23
C. Event rate and beam time calculation	24
D. New beamline	25
E. Increasing the quadrupole density in the FODO section	26
F. New backward-decay beamline concept	27
G. Opening the inflector ends	29
VI. Measurement of the Magnetic Field	30
A. Methods and Techniques	30
B. Past improvements	33
C. Future refinement	34
VII. ω_a Measurement	35
A. Overview	35
B. Electromagnetic Calorimeters	37
1. The E821 calorimeters	37

2. New segmented calorimeters for P969	39
C. New front scintillator hodoscope–FSH	41
D. Waveform digitizers	41
E. Data Acquisition	43
F. Systematic uncertainties on ω_a	45
1. Gain changes and energy-scale stability	46
2. Lost muons	47
3. Pileup	48
4. Coherent Betatron Oscillations	50
5. Electric field and pitch correction	51
6. ω_a systematic uncertainty summary	51
VIII. Manpower	53
IX. Resources and Costs	53
X. Timescale	54
XI. Summary of the Request	54
References	55
A. New Beamline Concept	59
a. Quad Doubling	59
b. Backward Decay Beam	61
c. Summary of Design	67
B. Beam Dynamics and Scraping	68
1. The Kicker and Quadrupoles	68
2. Beam Dynamics in the Ring	68
3. Oscillating Dipole Method of Scraping[66]	71
4. Pulsed Octupole Method to Remove the CBO[67]	73
C. The Superconducting Inflector	77
D. New Calorimeters	81

I. EXECUTIVE SUMMARY

The E821 experiment achieved a final uncertainty on the measurement of the muon anomalous magnetic moment a_μ of 0.54 ppm. The uncertainty is dominated by the statistical error of 0.46 ppm. This suggests that a further increase in precision is possible if a higher muon storage rate can be obtained. We propose to measure a_μ to an uncertainty of 0.2 ppm, derived from a 0.14 ppm statistical sample and equal total systematic uncertainties of 0.1 ppm from the measurement of the magnetic field and the extraction of the precession frequency. Ten times more events compared to E821 are needed. We expect to obtain a 5 times higher muon flux using a redesigned pion / muon beamline, to run for 16 continuous weeks, and to start our fits earlier because of elimination of the hadronic flash. Segmenting the detectors, replacing the waveform digitizers, and using a modern data acquisition system are necessary to handle the higher data rates. Improvements in the field-measuring system are also required.

The new beamline involves a 5.32 GeV/ c front end to collect positive pions, a doubling of the quadrupole lattice in the decay section, the same 3.094 GeV/ c final momentum selection section, and a new inflector having open ends. With the AGS operating at 60 TP/cycle, a fivefold increase in stored muons per hour is expected. At this rate, the statistics can be collected in 1600 h. An additional 500 h are required for setup.

Our planning envisions a development period lasting two years after scientific and funding approval. During this time, the beamline would be rebuilt and the detectors will be constructed. The parasitic pulse-on-demand mode can be used to commission the new beamline, develop final tunes, and debug and calibrate detectors. A 3-week engineering run is requested to accumulate a data set to study systematic uncertainties. One year later, we request a 21-week run to carry out the measurement.

II. INTRODUCTION

The magnetic dipole moment associated with a charged spin-one-half particle is related to the anomalous magnetic moment $a \left(\frac{e\hbar}{2m} \right)$ by

$$\vec{\mu}_s = g_s \left(\frac{e}{2m} \right) \vec{s}, \quad \mu = (1 + a) \frac{e\hbar}{2m}, \quad a = \frac{g - 2}{2}. \quad (1)$$

The large anomaly of the proton ($a = 1.79$) is a result of its internal structure, whereas the leptons e , μ and τ have anomalies which are expected to arise only from radiative corrections. The lowest-order radiative correction gives $a = \alpha/2\pi$, which is $0.0011614 \dots$, and dominates the anomaly of these leptons.

For a lepton, the standard model value of a has contributions from three types of radiative processes: QED loops containing leptons (e, μ, τ) and photons; hadronic loops containing hadrons in vacuum polarization loops; and weak loops involving the weak gauge bosons W, Z , and Higgs. Thus

$$a_{e,\mu}(\text{SM}) = a_{e,\mu}(\text{QED}) + a_{e,\mu}(\text{hadronic}) + a_{e,\mu}(\text{weak}).$$

A difference between the experimental value and the standard model prediction would signify the presence of new physics beyond the standard model. Examples of such potential contributions are lepton substructure, extra gauge bosons, anomalous $W - \gamma$ couplings, or the existence of supersymmetric partners of the leptons and gauge bosons.[1, 2]

The electron anomaly is now measured and calculated to a relative precision of about four and seven parts per billion (ppb) respectively,[4] with the theory error dominated by the uncertainty on the fine-structure constant. The electron anomaly provides one of the real triumphs of experimental and theoretical physics, especially QED. Because the independent measurements of α are less precise (7.4 ppb) than the present precision on the electron anomaly, the measurement of a_e has been used to determine the best measurement of the fine-structure constant.[5] The uncertainty in α is not an issue for a_μ because a_μ is measured to 0.5 parts per million (ppm), much less precisely than α .[3]

The relative contributions of heavier particles to a_μ compared to a_e scales as $(m_\mu/m_e)^2$, so the muon has a sensitivity factor of about 40,000 over the electron to higher mass scale radiative corrections. Thus muon ($g-2$) has an overall advantage of two orders of magnitude in measurable sensitivity to higher mass scales, including new physics. Thus muon ($g - 2$) represents an excellent opportunity to search for physics beyond the standard model.

The muon ($g - 2$) experiment, E821 began in the mid 1980s. A formal proposal was submitted to the Laboratory in fall 1985, and final approval was granted in spring 1988. The storage ring magnet reached full power in the summer of 1996 and muons were first stored in the ring in 1997. After engineering runs in 1997 and 1998, we collected large samples of data in each of three years: 1999 (1 billion e^+), 2000 (4 billion e^+), and 2001 (4 billion e^-), and all results have been published.[3, 6–9] The apparatus is documented in the literature.[10–19] Assuming *CPT* symmetry, the combined total relative error on the muon’s anomalous magnetic moment is ± 0.5 ppm, an improvement of a factor of 15 over the previous CERN experiments.[21]

The motivation for E821 was to observe the electroweak contribution from virtual W and Z^0 bosons, and to search for physics beyond the standard model such as supersymmetry, or muon substructure.[1, 2] Now that LEP has probed standard model radiative corrections, including the electroweak loop contributions, the present interest in muon ($g - 2$) is on its sensitivity to physics beyond the standard model and its ability to place restrictions on potential new physics.

With the publication of our paper in 2001, which indicated a 2.6 standard deviation difference with the standard model,[8] our experiment has generated intense, and continued interest in the community, and our progress has been followed in both the popular and scientific press. The final result from E821 differs by ~ 2.4 standard deviations from the theoretical prediction using e^+e^- annihilation into hadrons to determine the lowest order hadronic contribution.

Simultaneously with our progress in measuring a_μ more precisely, the knowledge of the standard model value of a_μ has improved from ± 5 ppm in 1983 to $\sim \pm 0.7$ ppm today. Further improvements are on the horizon, and will be discussed below.

We propose to measure muon ($g - 2$) to the limit of the present experimental technique, which can be achieved at Brookhaven in a reasonable running time. This improvement, along with the anticipated progress on the theory side will more than double our ability to constrain, or point to, new physics. The observation of a clear signal indicating physics beyond the standard model, or the new limits that we will be able to set, will be extremely important to our field.

III. E821 REVIEW

Experimentally we measure the spin precession relative to the momentum vector of a muon moving in a magnetic storage ring. With the assumption that the velocity is transverse to the magnetic field, the difference frequency between the spin and momentum precession in the storage ring, $\omega_a = \omega_S - \omega_C$, is given by

$$\vec{\omega}_a = -\frac{e}{mc} \left[a_\mu \vec{B} - \left(a_\mu - \frac{1}{\gamma^2 - 1} \right) \vec{\beta} \times \vec{E} \right], \quad (2)$$

where an electric field does not contribute to the spin motion for $\gamma = 29.3$. This value of γ is called the “magic” γ , and the magic muon momentum is $p_{magic} = 3.094$ GeV/c. We use electrostatic quadrupoles for vertical focusing. The storage ring is operated as a weak focusing ring, and we ran with field indices of $n = 0.142, 0.137$ and 0.122 during our three main periods of data collection.

As can be seen from Eq. 2, both ω_a and the magnetic field B must be known to extract a value of a_μ from the experiment. The field is measured with NMR techniques, and has been shimmed to ± 1 ppm uniformity when averaged over azimuth. Contour maps of the field averaged over azimuth are shown for the 2000 (μ^+) and 2001 (μ^-) running periods in Fig. 1. The B which appears in Eq. 2 is the field averaged over the muon spatial distribution in the ring. With such a uniform field, only modest information is needed on the muon distribution. In our data set from 2000 and 2001, the systematic error from uncertainties in our knowledge of the magnetic field weighted by the muon distribution was ± 0.03 ppm.[3, 9]

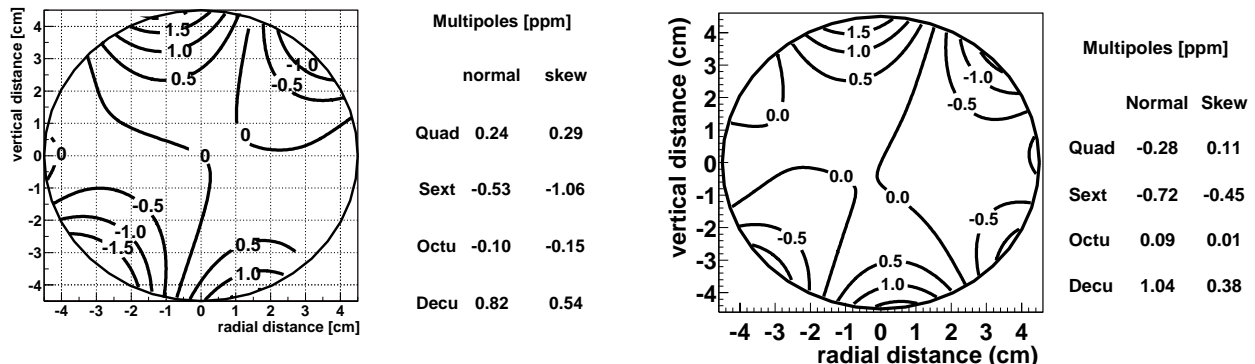


FIG. 1: Contour plots of the magnetic field from the 2000 run with μ^+ (left-hand side) and from the 2001 run with μ^- (right-hand side). The multipole content is shown for each contour plot.

To monitor the magnetic field during data collection, 366 fixed NMR probes were placed

around the ring and continuous readings from about 150 probes were used to track the field in time. About twice per week, a trolley with 17 NMR probes was used to map the field in the storage ring. During muon data collection, the trolley is stored in a garage inside the vacuum chamber. The trolley probes were calibrated with a special spherical water probe, which provides a calibration to the free proton spin precession frequency ω_p .

Positrons (electrons) from the parity violating decay

$$\mu^{+(-)} \rightarrow e^{+(-)} + \nu_e(\bar{\nu}_e) + \bar{\nu}_\mu(\nu_\mu) \quad (3)$$

are detected in lead-scintillating-fiber calorimeters[18] where the energy and arrival time are measured. The highest energy positrons (electrons) carry the spin information, and the number of high-energy positrons (electrons) above an energy threshold E_{th} as a function of time is given by

$$N(t) = N_0(E_{th})e^{-t/\gamma\tau} [1 + A(E_{th}) \sin(\omega_a t + \phi_a(E_{th}))]. \quad (4)$$

The uncertainty on ω_a is given by

$$\frac{\sigma\omega_a}{\omega_a} = \frac{\sqrt{2}}{\omega_a\tau_\mu\sqrt{NA}} \quad (5)$$

where the energy threshold E_{th} is chosen to optimize the quantity NA^2 . In the analysis of the data, many small effects such as coherent beam motion in the storage ring must be included.[3, 8] The data from our 2001 run using μ^- are shown in Fig. 2. A least squares fit to the electron(positron) spectrum is used to extract the frequency ω_a as discussed in Ref.[3, 8, 9]

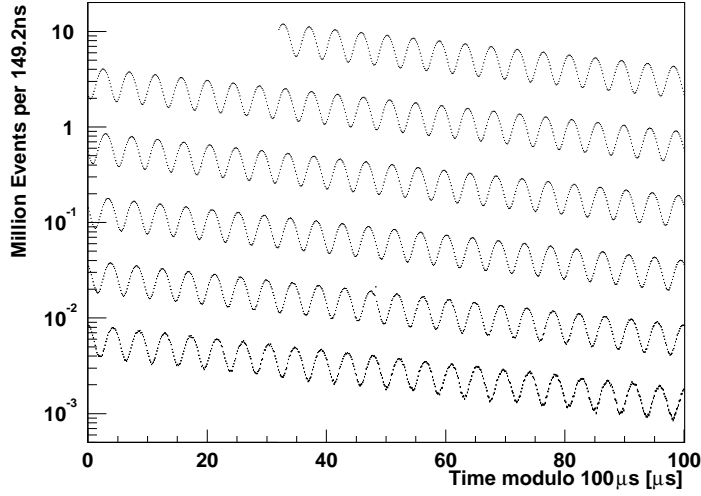


FIG. 2: The time spectrum of electrons from muon decay obtained in the 2001 running period. There are 4×10^9 events in the histogram.

Our final results are

$$a_{\mu^+} = 11\,659\,203(8) \times 10^{-10} \quad (0.7\text{ppm}) \quad (6)$$

$$a_{\mu^-} = 11\,659\,214(8)(3) \times 10^{-10} \quad (0.7\text{ppm}) \quad (7)$$

$$a_{\mu} = 11\,659\,208(6) \times 10^{-10} \quad (0.5\text{ppm}), \quad (8)$$

which will be compared to theory in the next section.

The key to any precision measurement is the systematic errors. The systematic and statistical errors from our 1999, 2000 and 2001 running periods[3, 8, 9] are given below in Table I, which shows clearly that E821 was statistics limited.

Data Run	B -Field (ω_p) Systematic Error (ppm)	Spin (ω_a) Systematic Error (ppm)	Total Systematic Error (ppm)	Total Statistical Error (ppm)
1999	0.4	0.3	0.5	1.3
2000	0.24	0.31	0.39	0.62
2001	0.17	0.21	0.27	0.66

TABLE I: Systematic and statistical errors from the three major E821 data collection runs.

The details of the systematic errors are given in Table II. Our goal is to improve the

systematic error on both ω_a and on ω_p (the magnetic field) to 0.1 ppm. These improvements will be discussed in detail in the following sections.

$\sigma_{\text{syst}} \omega_p$	1999	2000	2001	$\sigma_{\text{syst}} \omega_a$	1999	2000	2001
	(ppm)	(ppm)	(ppm)		(ppm)	(ppm)	(ppm)
Inflector Fringe Field	0.20	-	-	Pile-Up	0.13	0.13	0.08
Calib. of trolley probes	0.20	0.15	0.09	AGS background	0.10	0.01	‡
Tracking B with time	0.15	0.10	0.07	Lost Muons	0.10	0.10	0.09
Measurement of B_0	0.10	0.10	0.05	Timing Shifts	0.10	0.02	‡
μ -distribution	0.12	0.03	0.03	E-field/pitch	0.08	0.03	‡
Absolute calibration	0.05	0.05	0.05	Fitting/Binning	0.07	0.06	‡
Others [†]	0.15	0.10	0.07	CBO	0.05	0.21	0.07
				Beam debunching	0.04	0.04	‡
				Gain Changes	0.02	0.13	0.12
Total for ω_p	0.4	0.24	0.17	Total for ω_a	0.3	0.31	0.21

TABLE II: Systematic Errors from the 1999, 2000 and 2001 data sets.[3, 8, 9] CBO stands for coherent betatron oscillations. The pitch correction comes from the vertical betatron oscillations, since $\vec{\beta} \cdot \vec{B} \neq 0$. The E-field correction is for the radial electric field seen by muons with $p_\mu \neq p_{\text{magic}}$.

[†]Higher multipoles, the trolley frequency, temperature, and voltage response, eddy currents from the kickers, and time-varying stray fields

[‡]In 2001 AGS background, timing shifts, E field and vertical oscillations, beam debunching/randomization, binning and fitting procedure together equaled 0.11 ppm

IV. THE STANDARD MODEL VALUE OF THE ANOMALY

As mentioned above, the standard model value of a_μ has three contributions from radiative processes: QED loops containing leptons (e, μ, τ) and photons; hadronic loops containing hadrons in vacuum polarization loops; and weak loops involving the weak gauge bosons W, Z , and Higgs. Thus

$$a_{e,\mu}(\text{SM}) = a_{e,\mu}(\text{QED}) + a_{e,\mu}(\text{hadronic}) + a_{e,\mu}(\text{weak}).$$

Each of these contributions is discussed below.

A. QED and Weak Contributions

The QED and electroweak contributions to a_μ are well understood.[2] The QED contribution to a_μ has been calculated through four loops, with the leading five loop contributions estimated. The present value is

$$a_\mu^{\text{QED}} = 11\,658\,472.07(0.04)(0.1) \times 10^{-10} \quad (9)$$

where the uncertainties are from the uncertainty on α and the 5-loop QED estimate.[2] The electroweak contribution from one and two loops is

$$a_\mu^{\text{EW}} = 15.4(0.1)(0.2) \times 10^{-10} \quad (10)$$

where the first error comes from hadronic effects in the quark triangle diagrams from the two-loop electroweak, and the latter comes from the uncertainty on the Higgs mass.[2]

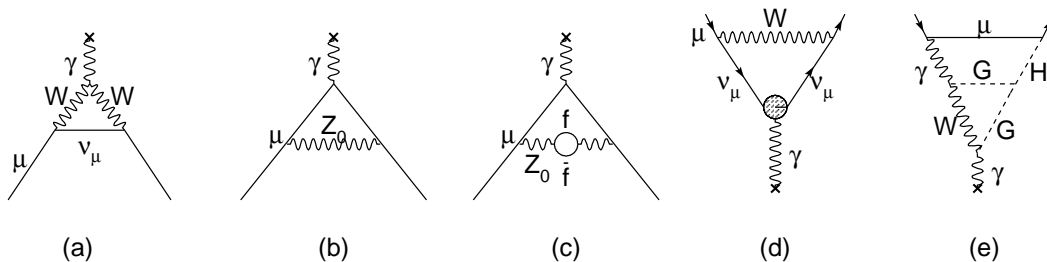


FIG. 3: Weak contributions to the muon anomalous magnetic moment. Single-loop contributions from (a) virtual W and (b) virtual Z gauge bosons. These two contributions enter with opposite sign, and there is a partial cancellation. The two-loop contributions fall into three categories: (c) fermionic loops which involve the coupling of the gauge bosons to quarks, (d) bosonic loops which appear as corrections to the one-loop diagrams, and (e) a new class of diagrams involving the Higgs where G is the longitudinal component of the gauge bosons. See Ref. [23] for details. The \times indicates the virtual photon from the magnetic field.

B. The Hadronic Contribution

The hadronic contribution to a_μ is about 60 ppm of the total. With its accuracy of 7.3 ppm, the CERN experiment[21] observed the contribution of hadronic vacuum polarization

shown in Fig. 4(a) at the 8 standard deviation level.

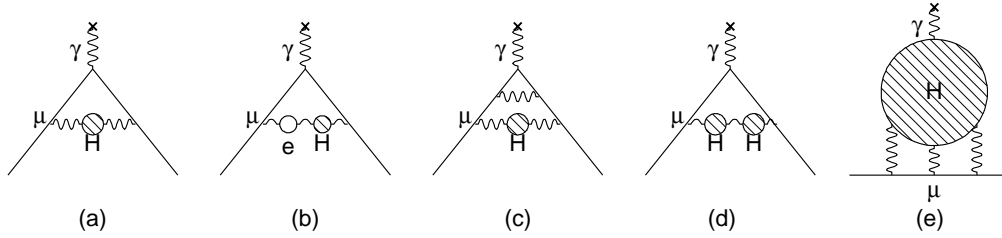


FIG. 4: The hadronic contribution to the muon anomaly, where the dominant contribution comes from the lowest-order diagram (a). The hadronic light-by-light contribution is shown in (e).

The largest contribution $a_\mu^{\text{had;LO}}$ comes from Fig. (4;a). The energy scale for the virtual hadrons is of order $m_\mu c^2$, which means this contribution must be calculated from the dispersion relation shown pictorially in Fig. 5. The measured cross sections for $e^+e^- \rightarrow \text{hadrons}$ are input for

$$a_\mu^{\text{had;LO}} = \left(\frac{\alpha m_\mu}{3\pi} \right)^2 \int_{4m_\pi^2}^{\infty} \frac{ds}{s^2} K(s) R(s), \quad \text{where} \quad R \equiv \frac{\sigma_{\text{tot}}(e^+e^- \rightarrow \text{hadrons})}{\sigma_{\text{tot}}(e^+e^- \rightarrow \mu^+\mu^-)}, \quad (11)$$

where $K(s)$ is a kinematic factor. This dispersion relation relates the bare cross section for electroproduction of hadrons to the hadronic vacuum polarization contribution to a_μ . Because the integrand contains a factor of s^{-2} , the values of $R(s)$ at low energies (the ρ resonance) dominate the determination of $a_\mu^{\text{had;LO}}$.

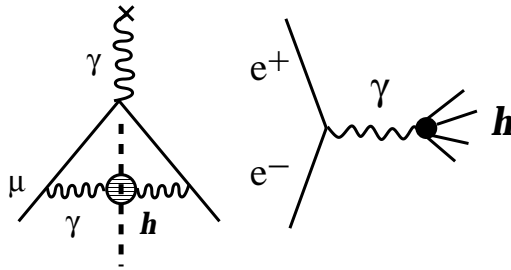


FIG. 5: The “cut” hadronic vacuum polarization diagram and the electroproduction of hadrons.

Because the cross sections at low energies dominates the dispersion relation, until very recently the hadronic contribution was primarily determined by one experiment, CMD2 at Novosibirsk.[24, 25] Several authors have used these data along with higher energy data from other experiments to determine $a_\mu^{\text{had;LO}}$. [26, 27] Given the importance of these data to

the interpretation of E821, other groups have embarked on separate programs to measure R . At Frascati, the KLOE collaboration has recently finalized their first measurement of the hadronic cross section up to the ϕ using initial state radiation to vary the center of mass energy.[28, 29] These results agree with the CMD2 data, both for the integral over the ρ in the dispersion relation, and for the shape of the pion form factor, which can be seen in Fig. 6. The effect of these new data on the standard model value is shown in Fig. 7.

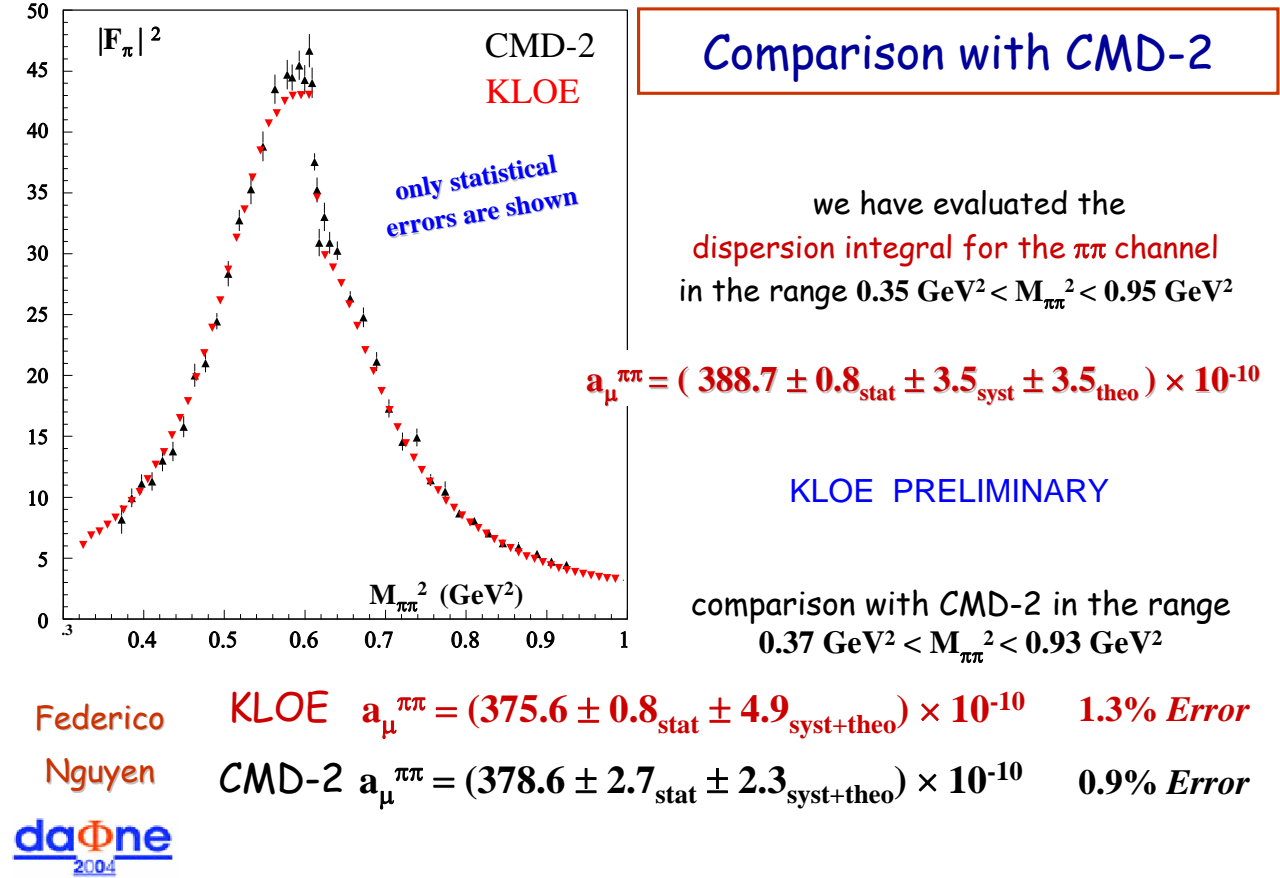


FIG. 6: Data from KLOE compared with CMD2, taken from F. Nguyen’s presentation at the daΦne workshop.[29] Note that the shape of the two data sets above the ρ is identical. These results are now final.[28]

Federico Nguyen
 daφne workshop, 6/04

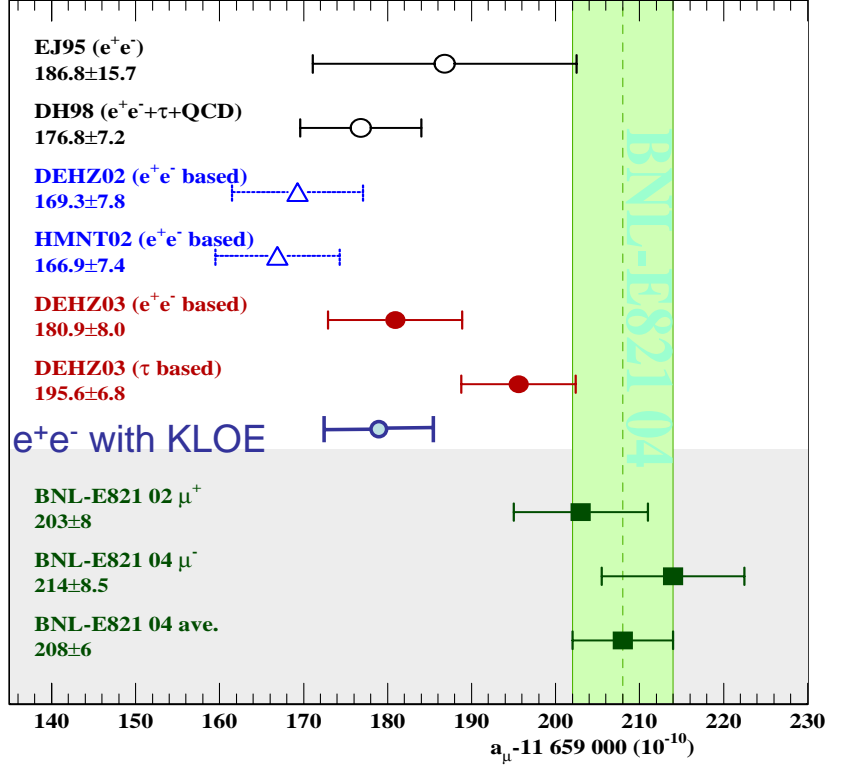


FIG. 7: Comparison of theory and experiment[29] (following Davier, et al.,[26]) showing the addition of the new KLOE results on $e^+e^- \rightarrow \text{hadrons}$. [28] Theory values are shown in the top section, and E821 results are shown in the lower shaded portion. The new point including the final KLOE result[28] is shown in blue just above the shaded section.

C. $a_\mu^{\text{had};\text{LO}}$ from Hadronic τ decay?

The value of $a_\mu^{\text{had};\text{LO}}$ from threshold up to m_τ could in principle be obtained from hadronic τ^- decays (See Fig. 4), provided that the necessary isospin corrections are known. This was first demonstrated by Almany, Davier and Höcker.[30] Hadronic τ decays to an even number of pions such as $\tau^- \rightarrow \pi^- \pi^0 \nu_\tau$, can be related to e^+e^- annihilation into $\pi^+ \pi^-$ through the CVC hypothesis and isospin conservation (see Fig. 8).[26, 30, 31] The τ -data only contain an isovector piece, and the isoscalar piece present in e^+e^- annihilation has to be put in “by hand” to evaluate $a_\mu^{\text{had};\text{LO}}$. As discussed below, there are unresolved issues which make it difficult to use the τ data on an equal footing with the e^+e^- data.

The e^+e^- and τ -decay evaluations do not agree on the hadronic contribution to a_μ , the shape of the pion form factor, and if CVC and the e^+e^- data are used to predict the

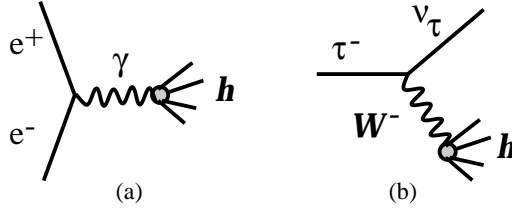


FIG. 8: Electroproduction of hadrons (a), and hadronic τ decay (b).

$\tau^- \rightarrow \pi^- \pi^0 \nu_\tau$ branching ratio, the value obtained is three standard deviations from the experimental value.[27] It has been speculated that a difference in the charged and neutral ρ masses could explain this difference.[33] Davier has pointed out that while assuming this mass difference fixes the shape problem, it causes a shift in normalization of 3.3% between the two.[34] While the shape difference goes away, this normalization difference moves the τ -based theory further away from the hadronic contribution obtained from the e^+e^- -based analysis. Marciano has argued that a modest mass difference, along with a full treatment of QED corrections to the width difference will remove part of the discrepancy, but a full QED calculation has not been carried out.[35]

Recently the KLOE collaboration[36] has measured the mass and width differences of the charged and neutral ρ . They find: $M_{\rho^0} - M_{\rho^\pm} = (0.4 \pm 0.7 \pm 0.6)$ MeV, and $\Gamma_{\rho^0} - \Gamma_{\rho^\pm} = (3.6 \pm 1.8 \pm 1.7)$ MeV. The mass difference is smaller than that favored by both Ghozzi and Jegerlehner,[33] or Davier.[34]

As stated by Davier and Marciano[2] in their review article to be published in Annual Reviews, “On one hand, it is clear that e^+e^- data are the natural input and that τ data need additional treatment to cope with isospin breaking corrections. On the other hand, recent history has taught us that reliability on the input data is an important concern and therefore redundancy is needed.” The data from CMD2 in Novosibirsk dominate the low-energy part of the dispersion relation, and until recently there was no independent check of their data. This check has now been carried out by the KLOE Collaboration (see Figs. 6 and 7).[28] Melnikov has strongly pointed out that the τ -decay data are not on an equal footing with the e^+e^- data, and he believes that the discrepancy between the two represents an unaccounted for isospin effect.[37] For similar reasons, Ghozzi and Jegerlehner also point out that, “the e^+e^- -data based evaluations are the more trustworthy ones.”[33] At this point there is almost general agreement that there are additional corrections which must be

included in the τ data before they can be treated on the same footing as the e^+e^- data in determining $a_\mu^{\text{had;LO}}$.

D. The Hadronic Light-by-light Contribution

The hadronic light-by-light contribution shown in Fig. (4;e) has been the focus of substantial theoretical investigation.[38, 39] This term must be calculated using a model, since it cannot be evaluated from data. The most recent calculation by Melnikov and Vainshtein obtained $13.6(2.5) \times 10^{-10}$ (0.22 ppm).[39] In their review,[2] Davier and Marciiano choose to quote a slightly lower value for this contribution, $12(3.5) \times 10^{-10}$ with an increased uncertainty. As discussed below, two groups are preparing a lattice calculation of this contribution.

E. Summary of the Standard Model Value and Comparison with Experiment

Davier and Marciiano have reviewed the theoretical prediction for the muon anomaly in a review for the 2004 edition of the Annual Reviews of Nuclear and Particle Physics.[2] We compare the E821 result with the standard model values from this review. The combined $\mu^+ \mu^-$ value from E821[3] and the e^+e^- -based standard model value are

$$a_\mu(\text{E821}) = 11\,659\,208(6) \times 10^{-10} \quad (0.5 \text{ ppm}), \quad (12)$$

$$a_\mu(\text{SM}) = 11\,659\,184(8) \times 10^{-10} \quad (0.7 \text{ ppm}) \quad e^+e^- \text{-based} \quad (13)$$

which give a difference of

$$\Delta a_\mu(\text{E821} - \text{SM}) = (24 \pm 10) \times 10^{-10}. \quad (14)$$

Use of the τ -decay data gives Δa_μ of $(8 \pm 9) \times 10^{-10}$. This comparison is shown graphically in Fig. 7 (taken from the KLOE collaboration), which uses the (slightly higher) standard model values from Davier, Eidelman, Höcker and Zhang.[27] The new e^+e^- based evaluation using both KLOE and Novosibirsk data is presented.

To show the sensitivity of muon ($g - 2$) to the electroweak gauge bosons, we subtract off the electroweak contribution given in Eq. 10 and we obtain

$$\Delta a_\mu = (39 \pm 10) \times 10^{-10}, \quad (15)$$

demonstrating a large sensitivity to virtual W and Z gauge bosons.

The present theoretical error is $\sim \pm 8 \times 10^{-10}$ (0.7 ppm) as reported by Davier and Marciانو,[2] who estimate that in the near future this error can be improved to $\sim \pm 4 \times 10^{-10}$ (0.35 ppm).

With the proposed experimental goal of 0.2 ppm uncertainty, the combined uncertainty for the difference between theory and experiment would be $\pm 4.6 \times 10^{-10}$, less than half that given above in Eq. 14.

F. Expected Improvements in the Standard Model Value

Much experimental and theoretical work is going on worldwide to refine the hadronic contribution. One reflection of this work is the conference held in Pisa, which brought together 57 participants who are actively working on parts of this problem, and these participants represented many additional collaborators. The poster for the conference is shown in Fig. 9.

Workshop on Hadronic Cross Section at Low Energy SIGHAD03

Pisa (Italy) - October 8-10, 2003

Advisory committee

- R. Barbieri (Pisa)
- D. G. Cassel (Cornell)
- M. Davier (Orsay)
- S. Eidelman (Budker Institute)
- P. Franzini (Roma)
- J. Gasser (Bern)
- M. Greco (Roma)
- F. Jegerlehner (Zeuthen)
- W. Kluge (Karlsruhe)
- J. Kühn (Karlsruhe)
- B. Lee Roberts (Boston)
- W. J. Marciano (BNL)
- T. Ohshima (Nagoya)
- G. Pancheri (LNF Frascati)
- K. R. Schubert (Dresden)
- L. Trentadue (Parma)
- Z. Zhao (U. Michigan)

Topics

- R measurements at present and future colliders
- Radiative corrections and Monte Carlo tools
- Hadronic contribution to a_μ and $\alpha_{em}(m_Z)$
- τ spectral functions and QCD
- Results from γPT
- Electroweak precision tests
- Measurement and theoretical evaluation of a_μ

Organizing committee

- F. Cervelli (Pisa)
- S. Di Falco (Pisa)
- V. Flaminio (Pisa)
- M. Incagli (Pisa)
- F. Nguyen (Roma)
- G. Venanzoni (Pisa)

Scientific secretariat

L. Lilli (sighad03@pi.infn.it)

<http://www.pi.infn.it/congressi/sighad03/>

INFN

UNIVERSITÀ DI PISA

FIG. 9: The poster advertising the workshop held in Pisa on the hadronic contribution to a_μ . There were 57 participants and 33 invited speakers.

With the confirmation of the CMD2 data by the KLOE collaboration, and the subsequent reduction in the error on the dispersion integral, we now discuss the ongoing work to further improve the e^+e^- data, and the efforts to use lattice QCD to calculate the strong interaction piece of a_μ . There are four e^+e^- efforts now underway: at Novosibirsk, at KLOE, at BaBar and at CLEO. Preliminary work has begun at Belle.

- **Novosibirsk:** The CMD2 collaboration continues to analyze their data and is expected to publish additional data covering a wider energy range and with smaller statistical errors. A modest improvement in $a_\mu^{\text{had;LO}}$ is expected from this extended data set, and it will provide an important check of the previously published data. The CMD2 collaboration is upgrading their detector to CMD3, and the VEPP2M machine is being upgraded to VEPP-2000. The maximum energy will be increased from $\sqrt{s} = 1.4$ GeV to 2.0 GeV. These upgrades will permit the cross section to be measured from threshold to 2.0 GeV using an energy scan. These new data will fill in the energy region between 1.4 GeV where the CMD2 scan ended, up to 2.0 GeV, which was the lowest energy point reached by the BES collaboration in their measurements. Their goal is to measure R directly to 0.2-0.3% precision in the ρ -meson energy region. If successful, VEPP-2000 will allow CMD3 to reach a precision below 0.35 ppm ($< 4 \times 10^{-10}$). These results can be expected in 5-8 years from now.
- **KLOE:** The KLOE collaboration has measured the hadronic cross section using initial-state radiation (ISR) to lower the CM energy from the ϕ where $\text{da}\phi\text{ne}$ operates. They have data over the rho resonance, which are shown in Fig. 6. They have additional data with systematic errors which are half of those for the data in Figures 6 and 7.[41] Their paper on the first data set has just been submitted[28] and work has begun on the analysis of the second data set.
- **BaBar:** The BaBar collaboration is measuring the hadronic cross section using ISR. Since the CM energy is much higher for BaBar than $\text{da}\phi\text{ne}$, the photon is hard, and easy to detect (in $\text{da}\phi\text{ne}$ the ISR photon goes down the beam pipe). Furthermore BaBar can measure $R(s)$ directly, since they also measure muon pairs. They are in the process of replacing their muon chambers, and over the next two years they will replace the chambers, and get substantial new data on $R(s)$.[42]

- **CLEO:** The CLEO collaboration has embarked on a measurement of $R(s)$ at higher energies. They have taken six points with high statistics in the energy range $\sqrt{s} = 7.0 - 10.33$ GeV, and 28 points with lower statistics in the energy range $\sqrt{s} = 11.15 - 11.39$ GeV. Their hope is to have these data analyzed and written up by the end of 2004. The data collection during much of the next year will be at 3.77 GeV, and they will explore the use of ISR to measure $R(s)$ at lower energies.[43]
- **Belle:** The Novosibirsk collaborators on Belle are exploring the possibility of using ISR to measure R . This work is in the preliminary stage.[44]
- **Calculations on the Lattice - Lowest-Order:** With the increased computer power available for lattice calculations, it may be possible for lattice calculations to contribute to our knowledge of the lowest order hadronic contribution. Blum has performed a proof-of-principle quenched calculation on the lattice.[45] He and his collaborators are continuing this work with an unquenched calculation which looks quite promising.[46, 47]
- **Calculations on the Lattice - Hadronic light-by-light:** The hadronic light-by-light contribution has a magnitude of 12×10^{-10} , ~ 1 ppm to a_μ , with an estimated error of about 0.3 ppm.[39] A modest calculation on the lattice would have a large impact. There are two separate efforts to formulate the hadronic light-by-light calculation on the lattice. Blum and his collaborators at BNL and RIKEN are working on the theoretical framework for a lattice calculation of this contribution.[47] A second effort led by K-F. Liu is beginning to work on an independent calculation of this contribution, and they plan to formulate the calculation for the lattice over the next few months.[48]

G. Physics Beyond the Standard Model

For many years muon, $(g - 2)$ has played an important role in constraining physics beyond the standard model.[1, 2, 51] The interest with which our E821 results have been received by the community shows that this role continues.

If the muon is a composite fermion at some scale $\Lambda_\mu \gg m_\mu$ then there is a contribution

to its magnetic moment

$$\delta a_\mu(\Lambda_\mu) \simeq \frac{m_\mu^2}{\Lambda_\mu^2} \quad (16)$$

and any deviation from the standard model can be used to place a lower limit on muon substructure, a limit which is in the few TeV range.[49]

Searches have been carried out for anomalous gauge boson couplings in triple gauge boson vertices such as the $\gamma\gamma W$ vertex, which appears in the first-order electroweak loop shown in Fig. (3;a). The W magnetic moment can be parameterized as

$$\mu_W = \frac{e}{2m_W} (1 + \kappa + \lambda) \quad (17)$$

where in the standard model $\kappa = 1$ ($g_W = 2$) and $\lambda = 0$. To leading order[1]

$$a_\mu(\kappa, \lambda) \simeq \frac{G_F m_\mu^2}{4\sqrt{2}\pi^2} \left[(\kappa - 1) \ln \frac{\Lambda^2}{m_W^2} - \frac{1}{3}\lambda \right]. \quad (18)$$

and the electric quadrupole moment is given by

$$Q_W = -\frac{e}{m_W^2} (\kappa - \lambda). \quad (19)$$

LEP2, CDF and D0 have restricted the values of $\Delta\kappa$ and $\Delta\lambda$, and the present limits given in the Particle Data Tables[50] restrict a one-standard-deviation discrepancy from a nonstandard $W\gamma\gamma$ coupling to $a_\mu(\text{new physics}) \lesssim 0.3$ ppm. Thus any disagreement which might have been observed between the standard model value and E821 of the magnitude shown in Eq. 14 could not be explained by anomalous $W\gamma\gamma$ couplings.

Were they to exist, muon ($g-2$) would have substantial sensitivity to the supersymmetric partners to the W and Z bosons. The SUSY diagrams for the magnetic dipole moment, the electric dipole moment, and the lepton-number violating conversion process $\mu \rightarrow e$ in the field of a nucleus are shown pictorially in Fig. 10. In a generic model with equal SUSY masses the supersymmetric contribution to a_μ is given by[40]

$$a_\mu(\text{SUSY}) \simeq \frac{\alpha(M_Z)}{8\pi \sin^2 \theta_W} \frac{m_\mu^2}{\tilde{m}^2} \tan \beta \left(1 - \frac{4\alpha}{\pi} \ln \frac{\tilde{m}}{m_\mu} \right) \quad (20)$$

$$\simeq (\text{sgn}\mu) 130 \times 10^{-11} \tan \beta \left(\frac{100 \text{ GeV}}{\tilde{m}} \right)^2 \quad (21)$$

$$\simeq 1.31 \text{ ppm} \tan \beta \left(\frac{100 \text{ GeV}}{\tilde{m}} \right)^2 \quad (22)$$

$$(23)$$

which indicates the dependence on $\tan\beta$ (the ratio of the vacuum expectation values of the two Higgs fields) and the SUSY mass scale. Thus muon $(g-2)$ is sensitive to any SUSY model with large $\tan\beta$. If supersymmetry were to be discovered at the LHC and the SUSY mass spectrum measured, the value of a_μ will continue to be important. In that case, the value of a_μ would provide the best measurement of $\tan\beta$ (at the $\sim 20\%$ level).

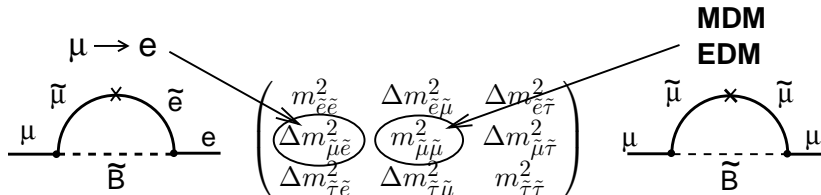


FIG. 10: The supersymmetric contributions to the anomaly, and to $\mu \rightarrow e$ conversion, showing the relevant slepton mixing matrix elements. The MDM and EDM give the real and imaginary parts of the matrix element, respectively. The \times indicates a chirality flip.

The anomalous magnetic moment of the muon is sensitive to contributions from a wide range of models beyond the standard model, and will continue to place stringent restrictions on them. This unique sensitivity to new physics is what motivates our collaboration to push forward with a new measurement.

V. A NEW $(g-2)$ EXPERIMENT

A. Scientific Goal

Our measurement of a_μ in BNL Experiment E821 included data from four muon-injection running periods and one short pion-injection run. A statistical uncertainty of 0.46 ppm, combined in quadrature with systematic uncertainties from the magnetic field measurement (0.17 ppm) and spin-precession analysis (0.21 ppm) yields the final overall uncertainty of 0.54 ppm. The result is statistics limited. We believe an improvement by a factor of 2.5—giving an uncertainty in a_μ of 0.2 ppm—is both scientifically compelling and technically achievable. To do so in a single production run will require an increase in muon flux by a factor of 5, a reduction in systematics by a factor of 2, and a reduction in background. The plan described below will achieve these stated goals.

The concept of the measurement remains unchanged from E821 but includes both incremental upgrades and qualitative changes. A new injection scheme will increase the muon flux and eliminate the hadron-induced background. To handle the higher event rates, the detectors, electronics and data acquisition systems will be replaced. Improvements in the storage ring field uniformity and its measurement system follow a plan of continuous small improvements started some years ago. A complementary method of data collection and analysis, which is immune to pileup, has been identified. It will be pursued in parallel to our traditional technique. The overall changes do not rely on untested technology nor do they require lengthy R&D; however, significant beamline design will be required.

B. Strategy of a new experiment

The key to a new measurement is increasing the muon flux. We have identified two areas where changes will result in a higher stored muon rate. Increasing the number of quadrupoles in the straight decay section of the beamline by a factor of 2 – 4 results in an increase in muon flux by the same factor. Ample space exists and the quads are relatively inexpensive. Muons entering the storage ring pass through an inflector having closed ends. Scattering and energy loss reduces the stored muon fraction by a factor of 2. We have built and tested a prototype inflector having an open end; a full-size inflector having both ends open will be built for the new experiment. An increase in the stored muon fraction by a factor of 2 is expected. We plan to use a high-momentum front end in our beamline so that backward-decay muons can be collected rather than forward-decay muons. The front-end momentum of 5.32 GeV/ c produces 180-degree decay muons at exactly the magic momentum of 3.094 GeV/ c . The mismatch in pion and muon momentum is so large that no pions will make the final bend into the storage ring. The hadron-induced flash will be absent. We are not yet able to predict a flux increase (or decrease) factor at this time from this major change. Preliminary Monte Carlo calculations suggest the factor will be close to the current forward-decay transmission. We adopt a factor of 1 for planning purposes in this proposal. At this stage, we have confidence that our goal of $\times 5$ more stored muons can be achieved by a combination of AGS running at 60 TP, increased number of quadrupoles, a new inflector, and the use of the backward beam. This rate increase is used to establish rates for detectors, electronics, data acquisition and in the request for run time. The final optimization of the

new beamline design will require assistance and consultation with experts from the AGS.

The commissioning plan assumes parasitic operation during one AGS/RHIC running cycle where “pulse-on-demand” can be used to establish the new beamline tunes and test all aspects of the experiment. Pulse-on-demand was very effective in the early stages of E821. A 3-week dedicated period, at the end of this running cycle, is requested to study systematic errors. A 21-week production run is requested one year later.

C. Event rate and beam time calculation

Our goal of $\delta a_\mu = \pm 0.2$ ppm is obtained from a statistical uncertainty of 0.14 ppm and equal systematic uncertainties of 0.1 ppm each for the field and precession analyses. The required running time at the assumed rate is outlined in Table III. Experience suggests that 5 weeks of setup time with beam available is required before “good” data is obtained.

Table III includes the factors and comments.

TABLE III: Event rate calculation for P969.

Value	Factor	Comment	Note
7×10^{10} events	–	Required number of fitted events	1
10.3×10^{10}	$\times 1.47$	Corrected to $t = 0$	2
8.6×10^{11} stored μ	$\times 0.12$	Positrons accepted with $E > 1.8$ GeV	3
7.2×10^7 fills	$\times (1/12,000)$	Stored muons per fill at 60 TP	4
1.7×10^7 fills	$\times 4$	Flux increase: quad doubling and new inflector	5
1125 h	$\times (1/1.6 \times 10^4)$	Standard AGS 12 fills per 2.7 s cycle	6
1600 h	$\times (1/0.7)$	Experiment data-collection uptime (actual)	7
500 h	–	Setup time before “smooth” data taking	8
2100 h	–	Total beam hours requested for main run	9
21 weeks	$\times 0.01$	Average delivered beam of 100 h/week	10

Notes explaining entries in Table III:

1. Required number of events in the fit. We assume fit start time is $25 \mu\text{s}$ after injection, see Eq. 5.

2. Projecting back to injection increases the effective required event count by a factor of 1.47.
3. Fraction of decay positrons with energy above 1.8 GeV and detected by the calorimeters.
4. The number of storage ring fills required at 12,000 stored muons per fill. The stored muon number is based on measurements in E821 and an assumed average AGS intensity of 60 TP/cycle.
5. The increase in stored muon flux by a factor of 4 from doubling the number of quads and replacing the inflector. The final factor will depend on the actual quadrupole increase and the muon yield using a high-momentum front end.
6. At 12 fills per 2.7 s AGS cycle, this gives the number of hours of continuous data taking required.
7. Assumes 70% uptime, a value based on our previous experience during smooth production running.
8. Standard setup time (as realized in the past) to adjust tunes, optimize stored muon flux, measure vertical profiles, make final detector calibrations, and other preliminary steps.
9. Total number of hours requested for the production run.
10. Weeks required, assuming 100 h of delivered beam per week. This may vary depending on the sharing efficiency with RHIC.

D. New beamline

A central feature of this proposal is a redesign of the pion / muon beamline channel. The present E821 beamline is optimized for pion production and transport at approximately 3.1 GeV/ c . A momentum selection is made at a dispersive focus immediately downstream of the production target at the K1/K2 collimators and a second momentum selection is made just upstream of the muon storage ring at the K3/K4 collimators (see Fig. 11). An

80 m long straight section exists between these bends. It is sparsely occupied by quadrupoles tuned in a standard focusing-defocusing (FODO) arrangement (depicted as open circles in the figure). Muons born from pion decay in this section can be captured and transported by the line. For muon injection, the first bend selects pions with momenta 3.114 GeV/ c and the second bend selects particles having 3.094 GeV/ c (the magic momentum, P_{magic}). The 1.7% mismatch in momentum is necessary to remove most of the pions at K3/K4. Still, a pion (and proton) flux approximately equal to that of the muons is transported into the storage ring. The vast majority of these hadrons crash into the storage ring steel and or the detectors and create a prompt “flash” in the detectors. The hadronic interactions also create neutrons, which thermalize and capture resulting in a continuous soft background. This background appears as a baseline (pedestal) shift, which decays with a time constant of tens of microseconds. The prompt and delayed flash are severe enough so that the detectors must be gated off at injection and turned on some tens of microseconds later. Because the flash limits the rate at which the experiment can be conducted, reducing or eliminating it is one of our most important goals.

E. Increasing the quadrupole density in the FODO section

Figure 12a illustrates the beam envelope modelled using the ray-trace program TRANSPORT [52]. The outer envelope extends into the physical quad structure, particularly in the top (vertical) panel; particles are lost. By doubling the number of quads, the beam’s physical envelope is reduced. Conservation of accepted emittance at the storage ring implies that larger muon decay angles will be accepted. Quad doubling in the FODO section keeps the entire envelope well contained as shown in Fig. 12b. The Monte-Carlo particle tracking program DECAY TURTLE [52] was used to model the change. An increase by a factor of 2.1 in transmitted muons is realized for a tune with a FODO section having twice the number of quadrupoles. Ample space is available and the relatively low cost of the 4-inch quads used gives us many options to modify the FODO section. Further studies are in progress to verify the expected flux increase from tripling or quadrupling the number of quads in this region. A final optimization will require assistance from AGS experts and a full cost analysis.

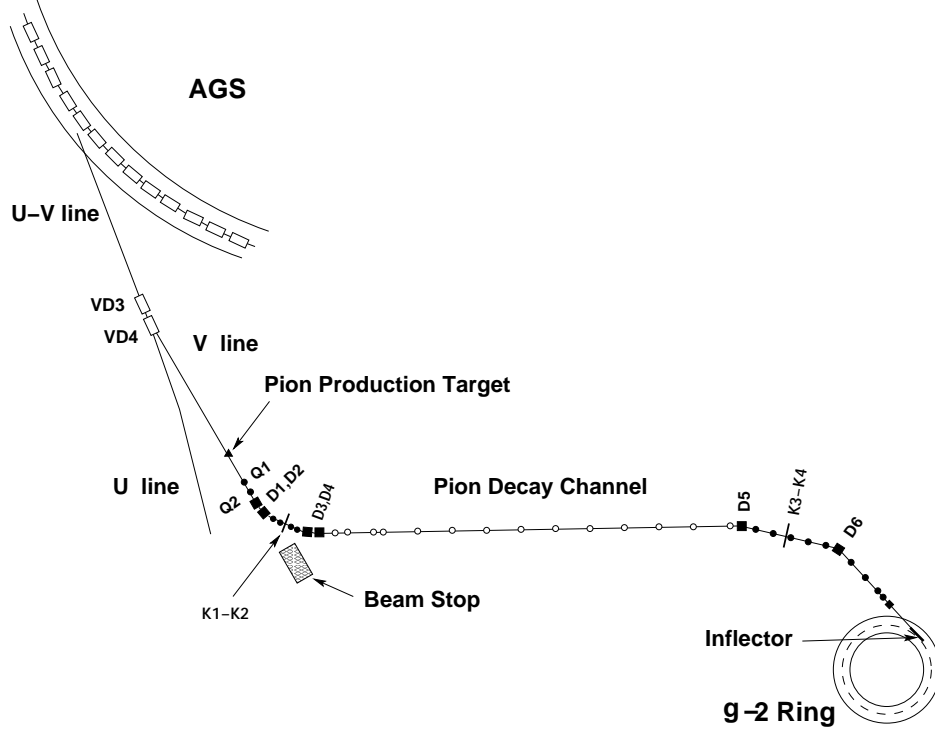
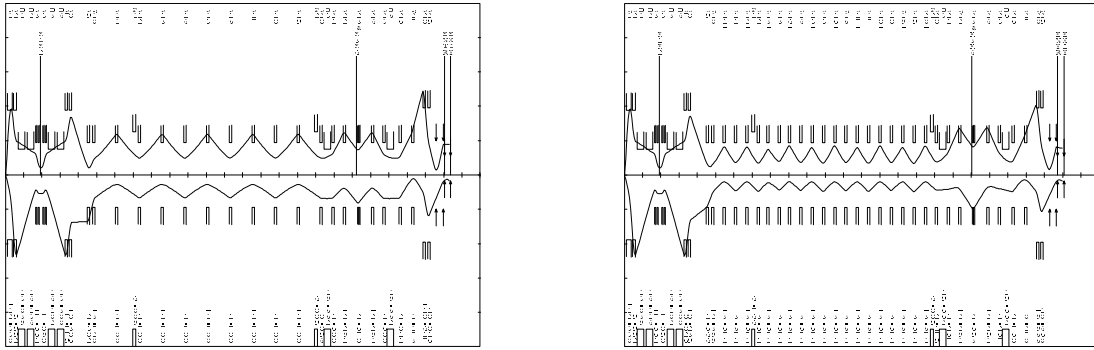


FIG. 11: Plan view of the pion/muon beamline.

F. New backward-decay beamline concept

The highest muon flux for a truly forward-decay beam occurs when the pion front end is tuned 0.5% above P_{magic} . However, this slight momentum difference permits a large number of pions to enter the storage ring. If the pion momentum is higher (leaving the muon selection section unaltered), both the pion and muon rates are reduced, but the pion rate drops faster. Acceptable operating conditions—ample flux, tolerable flash—occur when P_π is 1.7% above P_{magic} . The accepted muons are created slightly off axis from zero degrees.

Raising the pion momentum to 5.32 GeV/ c is a logical extension of this argument. At this momentum, the muons having the magic momentum are emitted at exactly 180 degrees. The mismatch in momentum at K3/K4 is maximized, implying that no pions (or protons) will enter the storage ring. The backward muons are transported and injected into the storage ring as usual (their spin direction is reversed, but their average polarization will be very close to unity). The hadronic flash will be absent so we expect to be able to avoid a sophisticated PMT gating circuit in the new detectors. Our phase-space-based studies suggest that a potential increase in the number of available muons exists, however, only



(a) Normal ($g - 2$) Tune

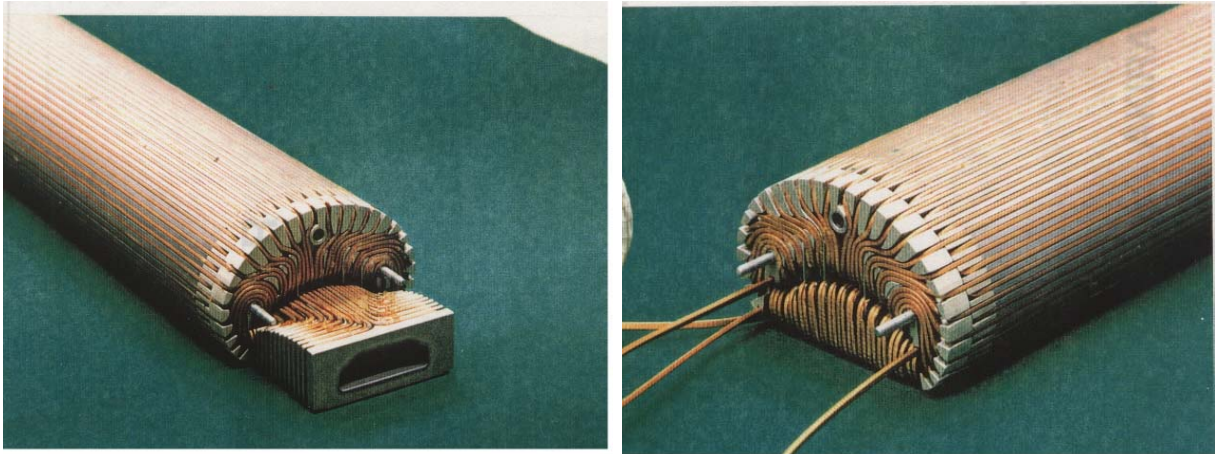
(b) Quad Doubling Tune

FIG. 12: TRANSPORT envelopes for the current beamline and one with double the number of quads in the FODO decay section. The top panels of each figure represent the vertical beam envelopes; the bottom panels represent the horizontal envelopes. When the envelope extends into the quad (depicted as rectangular boxes, particles are lost. The beam envelope is completely contained in in (b).

preliminary tune design work has been completed and no firm conclusions can yet be made.

We have discussed with key AGS personnel the implications of changing the front end to transport higher-momentum pions. Modification or replacement of certain elements are required. The work plan includes:

- Modification of the pole tips on the 18D72 dipoles D1, D3 and D4. Dipole D1 has been in a high-radiation environment and will likely be replaced. The modification will enable the dipoles to run at 25 kG.
- The “C”-shaped dipole D2 is a non-standard laboratory magnet designed for a field of 18 kG and open on one side to let the primary proton beam pass. To produce a field close to 23 kG, it must be replaced with one having significantly more return yoke.
- Quadrupoles Q1/Q2 are already running near maximum field gradient. To capture the pions at this momentum, Q1 must increase in length by 25% and the target position must be adjusted upstream by 33 cm.



(a) Open End

(b) Closed End

FIG. 13: Photos of the open- and closed-end inflector prototype.

G. Opening the inflector ends

The original superconducting inflector design for E821 included two options for the ends: open or closed, see Fig. 13. Both versions were built in 0.5 m long prototype form, but only the closed-end version was built at full scale (1.7 m length) and used in the experiment.[10, 11] The closed inflector was selected because of its simpler construction and was thought to be more stable against Lorentz forces. Further, the closed-end inflector has a smaller fringe field that could be more easily shielded from the storage ring field seen by the muons. On the downside, beam transport studies show that multiple scattering and energy loss in the closed end reduce the transmission by a factor of 2.

The stability of the open-ended coil configuration was demonstrated at full current in a 1.5 T magnetic field. Based on our measurements from E821 [11], the added leakage field from the open end can be excluded from the storage region by a passive superconducting sheet.

A factor of 2 increase in muon flux is expected from opening the ends. Much of the investment in engineering for this device has already been made and custom tooling necessary to construct the magnet exists. The inflector is discussed in detail in an appendix.

VI. MEASUREMENT OF THE MAGNETIC FIELD

We propose to measure the magnetic field in the present experiment to a precision of about 0.11 ppm using the same technique and apparatus which was used in E821. The technique was developed, implemented, and refined over a period of about twenty years.[16, 54–58]. An uncertainty of 0.17 ppm had been reached when experiment E821 was stopped (cf. table IV). A brief overview of the measurement is given in section VIA. Section VIB outlines the improvements that were made in the course of E821 and which resulted in the gradual reduction of the uncertainty in the field measurement by a factor of three. In section VIC we outline our plans for reestablishing the measurement after several years without operation, and how we foresee a further improvement in uncertainty by about 30% to a projected 0.11 ppm.

A. Methods and Techniques

The measurement of the magnetic field in experiment E821 is based on proton NMR in water. A field trolley with 17 NMR probes was moved typically 2–3 times per week throughout the entire muon storage region, thus measuring the field in $17 \times 6 \cdot 10^3$ locations along the azimuth. The trolley probes were calibrated *in situ* in dedicated measurements taken before, during, and after the muon data collection periods. In these calibration measurements, the field homogeneity at specific calibration locations in the storage region was optimized. The field was then measured with the NMR probes mounted in the trolley shell, as well as with a single probe plunged into the storage vacuum and positioned to measure the field values in the corresponding locations. Drifts of the field during the calibration measurements were determined by re-measuring the field with the trolley after the measurements with the plunging probe were completed, and in addition by interpolation of the readings from nearby NMR probes in the outer top and bottom walls of the vacuum chamber. The difference of the trolley and plunging probe readings forms an inter-calibration of the trolley probes with respect to the plunging probe, and hence with respect to each other. The plunging probe, as well as a subset of the trolley probes, were calibrated with respect to a standard probe[17] with a 1 cm diameter spherical H₂O sample in a similar sequence of measurements in the storage region, which was opened to air for that purpose. The standard probe is the same as

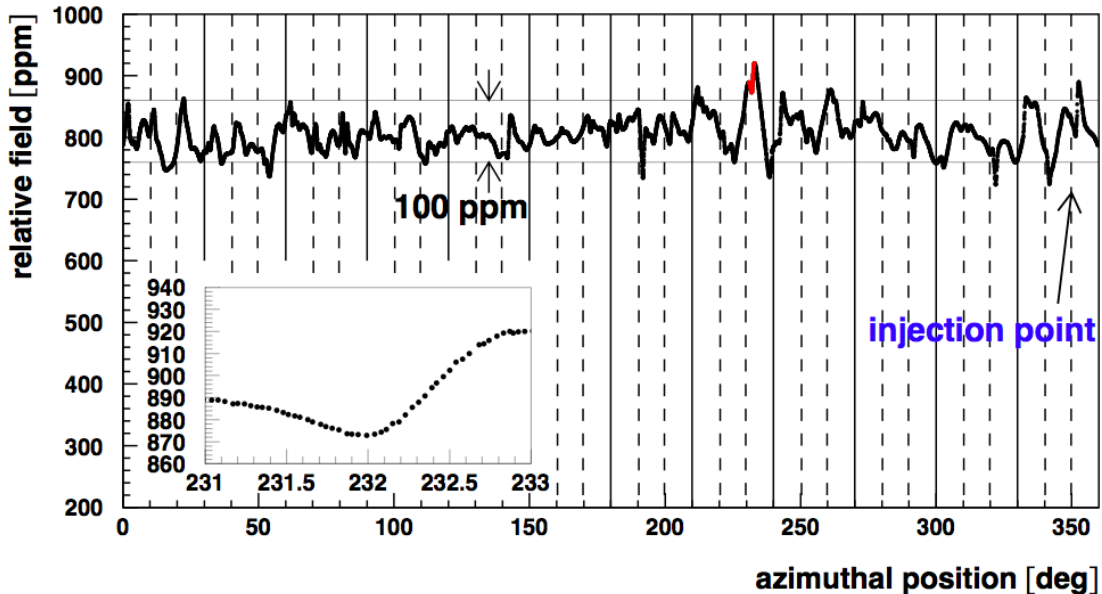


FIG. 14: The NMR frequency measured with the center trolley probe relative to a 61.74 MHz reference versus the azimuthal position in the storage ring. These data come from one of the 22 measurements taken with the field trolley during the 2001 data collection period. The solid vertical lines mark the boundaries of the 12 yoke pieces of the storage ring. The dashed vertical lines indicate the boundaries of the pole pieces.

the one used in the muonium measurements that determine the ratio λ of muon to proton magnetic moments[53]. The NMR clock and the clock that measured the muon spin precession period were phase-locked to the same LORAN-C[59] signal. Systematic effects include the instrument response and were extensively studied. The leading uncertainties in the calibration procedure resulted from the residual inhomogeneity of the field at the calibration locations, and from position uncertainties in the active volumes of the NMR probes.

The ring magnet design[12], the inflector design[10, 11], and extensive shimming contributed to the overall uniformity of the field throughout the storage ring. Figure 14 shows one of the magnetic field measurements with the center NMR probe in the trolley for E821's final data collection period in the year 2001. A uniformity of ± 100 ppm in the center of the storage region was achieved for both field polarities and for the full azimuthal range, in particular also in the region where the inflector magnet is located. Figure 15 shows a two-dimensional multipole expansion of the azimuthal average of the field in the muon stor-

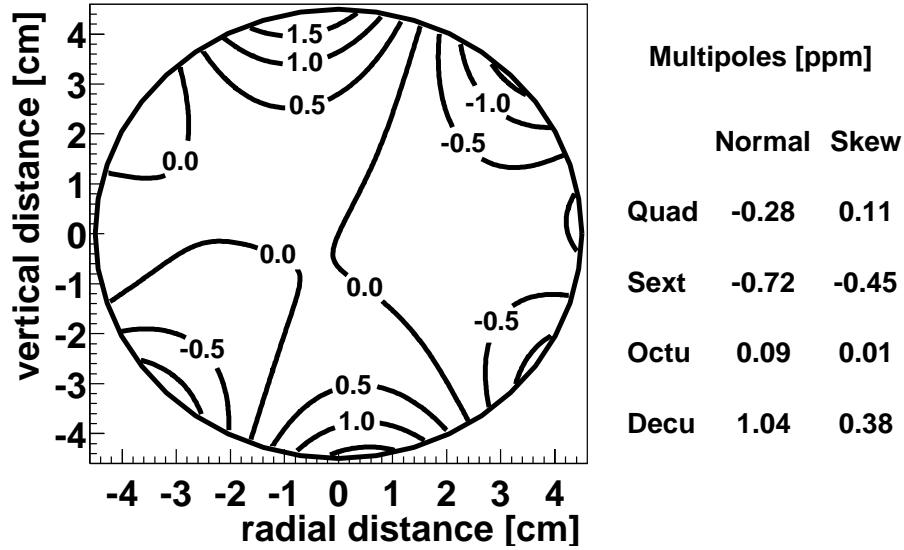


FIG. 15: A 2-dimensional multipole expansion of the azimuthal average of the field measured with trolley probes with respect to the central field value of about 1.45 T. The multipole amplitudes are given at the aperture of the 4.5 cm radius storage aperture.

age region from a typical trolley measurement in 2001. Since the average field is uniform to within 1.5 ppm over the storage aperture, the field integral encountered by the (analyzed) muons is rather insensitive to the profile and the precise location of the beam, which was determined to within a millimeter in both coordinates.

The measurements with the field trolley were used to relate the readings of about 150 (out of 370) NMR fixed probes in the outer top and bottom walls of the storage vacuum chamber to the field values in the beam region. The fixed NMR probes were read out continually. Their readings were used to interpolate the field during data collection periods, when the field trolley was parked in a garage inside of the vacuum chamber. The garage is located just outside the beam region. The uncertainty in this interpolation was estimated from redundant measurements with the field trolley within the same magnet-on period.

The field change induced by eddy currents from the pulsed kickers was measured for a prototype chamber with an optical magnetometer [13]. Time-varying stray fields from the accelerator were measured *in situ* with the NMR system [16, 55] and found to contribute negligible uncertainty. Another small uncertainty comes from the off-vertical field components [15].

The total field uncertainty is predominantly systematic, with the largest contribution coming from the calibration. For all data collection periods, the results and uncertainties were based on two largely independent analyses.

B. Past improvements

The uncertainty in the field measurement was improved by a factor of three in the course of experiment E821 and reached a final value of 0.17 ppm for the year 2001 (cf. Table IV).

The superconducting inflector magnet [11] was replaced between the data collection periods in 1999 and 2000 because of a damaged superconducting shield which permitted stray magnetic flux to leak into the storage region. This replacement minimized the inflector fringe field in the storage region in subsequent data collection periods and eliminated the need to measure the magnetic field with separate trolley settings in the inflector region. Together with refined shimming with programmable current loops, it improved the field homogeneity and thus reduced the uncertainty associated with our knowledge of the muon distribution that existed for our 1998 and 1999 results.

The addition of a plexiglass port and mirror setup to the storage ring before the 2000 data collection started, allowed us to precisely position the trolley shell at the location of a plunging probe without breaking the vacuum. It thus allowed us to make a relative calibration of the trolley probes with respect to the plunging probe during the data collection periods in 2000 and 2001, in addition to the calibrations made before and after each period.

Improvements in the alignment of the trolley rails throughout the storage ring and improvements in the trolley drive mechanism allowed us to measure the field with the trolley more often during the 2000 and 2001 data collection periods. Furthermore, we upgraded the readout of the trolley position in the storage ring before the data collection period in 2001 to reduce the uncertainty in the measurement of the average central field with the trolley.

Additional study of the trolley frequency, temperature, and voltage response resulted in sharper limits for our 2000 and 2001 results.

TABLE IV: Systematic uncertainties in the measurement of the magnetic field for experiment E821 (1998–2001) and our projections for a future effort. The uncertainty ”Others” groups uncertainties caused by higher multipoles, the trolley frequency, temperature, and voltage response, eddy currents from the kickers, and time-varying stray fields.

Source of errors	Size [ppm]				
	1998	1999	2000	2001	future
Absolute calibration of standard probe	0.05	0.05	0.05	0.05	0.05
Calibration of trolley probe	0.3	0.20	0.15	0.09	0.06
Trolley measurements of B_0	0.1	0.10	0.10	0.05	0.02
Interpolation with fixed probes	0.3	0.15	0.10	0.07	0.06
Inflector fringe field	0.2	0.20	-	-	-
Uncertainty from muon distribution	0.1	0.12	0.03	0.03	0.02
Others		0.15	0.10	0.10	0.05
Total systematic error on ω_p	0.5	0.4	0.24	0.17	0.11

C. Future refinement

The methods and techniques used in E821 are not fully exhausted; modest further refinement is feasible. We would focus our efforts on the following items.

- *in situ* measurement of the field change from kicker eddy currents [13].
- Extensive measurements with the magnetic field trolley, aiming in particular to better resolve the position of the active NMR volumes inside the trolley shell and to map out the response functions to the level where *corrections* can be applied, rather than *limits* be set.
- More frequent measurements of the magnetic field in the storage ring during beam periods (following mechanical maintenance on the trolley drive and garage).
- Repair and retuning of a number of the fixed NMR probes to improve the sampling of the storage ring.
- Solve the problem we had with the power supplies for the surface correction coils to eliminate the occasional data loss caused by oscillating outputs.

- Analysis refinements to reduce trolley position uncertainties in the storage ring.
- Temperature control of the environment of the storage ring magnet.

Better knowledge of the muon beam distribution, required by the anomalous precession measurement, would also benefit the measurement of the average magnetic field.

Continued development of an independent helium-3 based standard probe [60], would further benefit the field measurement, however, the projected uncertainty of 0.11 ppm does *not* rely on it. The same holds for extensive additional shimming of the storage ring.

We are confident that the goal of a field knowledge to a precision of 0.1 ppm can be reached using the existing experience in the field group. The present hardware has the potential to reach that level with the moderate aforementioned repairs and upgrades.

VII. ω_A MEASUREMENT

A. Overview

The stored muon flux, and consequently the rate, is expected to increase by a factor of 5 compared to E821. The existing detectors, electronics and data acquisition system are inadequate to handle this increase. As an example, the pileup fraction, which is already a concern in E821, will increase five fold in a monolithic calorimeter as is used presently. To maintain the pileup fraction at the current level, the detector must be segmented transversely. We describe a design below, which satisfies this requirement. The current waveform digitizers (WFD), operating with dual phase 200 MHz oscillators, store their digitized samples in an onboard memory, which is already limited in depth at the E821 data rates. We plan to use a single-phase WFD having a deeper onboard FIFO to avoid these difficulties. The current data acquisition system—based on mid-1990’s technology—must be greatly expanded to match the new electronics, high data rate, and significantly increased total data storage volume. We will adopt a standard system we are using at the Paul Scherrer Institute (PSI) in two related muon lifetime efforts—MuLan [62] and MuCap [63]—that closely match the demands from the new $(g - 2)$ effort. In addition to the changes in acquiring data, the data analysis effort will introduce a parallel method similar to that used in high-rate parity-violating experiments, which we describe below. The balance of two complementary methods to extract ω_a will continue our tradition of having multiple, independent approaches

to the data analysis. To do so adds specific data acquisition modifications, which we describe next.

Because the new ($g-2$) experiment will feature higher data rates, vulnerability to pileup-induced uncertainties and rate-dependent gain changes—for the existing detection system—will increase. To combat this, new segmented calorimeters will be built with segment size designed to maintain similar individual rates similar to those realized in E821. Naturally, shower spreading will introduce new challenges to event reconstruction and the gain monitoring system will have to be changed in concept to establish energy vs. time stability. The traditional, or T method, where individual decay-positron “events” are analyzed for time and energy, remains our primary standard analysis tool. Additionally, we will employ a complementary and elegant “integration” method, the Q method. This amounts to digitizing the energy deposited in an entire calorimeter (all segments) vs. time following injection. No threshold is necessary; all samples are recorded without bias. The method is robust and intrinsically immune to pileup.

In the T method, positron decays are recorded individually and are sorted by energy and time. For each positron recorded at time t and having energy greater than E_{th} , a single count is incremented in a histogram, such as the one shown in Fig. 2. The asymmetry is determined by the choice of threshold, and the statistical power is proportional to NA^2 . Optimizing this figure-of-merit implies setting E_{th} between 1.8 and 1.9 GeV. The T method is well understood by the current Collaboration; we employ it to determine event rates and running necessary for the goals of this proposal. A slight variant on the T method is an asymmetry-weighted (or energy-weighted) event mode, a T' method. Here, individual events having energy E_i are weighted by their asymmetry, A_i . This method improves the statistical power of the T method by about 10 percent at a cost of modestly increased demands on the gain stability of the detectors. The T' method can be derived from the standard data set and requires no additional hardware or special data-taking procedures. We have used variants of this method as part of the analysis approaches applied to the 2000 and 2001 data-taking periods in E821.

In contrast, the Q method does not rely on the separate identification or isolation of positron events. It involves integration of the energy deposited in the entire calorimeter and plotting the summed energy vs. time. In this simple method, the energy deposited, which is proportional to the light in the calorimeter, is digitized for the entire fill and the digitized

samples are in turn added from fill to fill to produce a final histogram. The histogram can be fit by the same function used to fit the T method data. The asymmetry is lower compared to the T method, but since all events are used N is larger. We have performed a **GEANT** simulation to compare the T and Q methods. The simulation is based on tracked muons through the storage ring and features details such as the coherent betatron oscillation, which modulates the detector acceptance. We ignored that small effect in fitting the data; the result is a poor χ^2/dof , but it otherwise does not affect the comparison. Figure 16 shows spectra prepared using the T and Q methods, both fit with the five-parameter function:

$$N \exp -t/\gamma\tau[1 + A \cos \omega t + \phi].$$

In the upper panel, the number of events having positron energy greater than $E_{th} = 1.8$ GeV is plotted vs. time after injection. The fit gives an uncertainty on ω_a of 59 ppm for this sample. The bottom panel shows the same simulation, but the plot represents calorimeter energy vs. time after injection. The uncertainty on ω_a is 65 ppm; the Q method is statistically weaker than the T method by about 9 percent, implying an 18 percent longer run is necessary to obtain the same precision. However, the Q method has an interesting advantage. There is no pileup correction to be made so the increased rate will not complicate the analysis algorithm. While the Q method had been recognized as viable during the E821 effort, it was impossible to implement with the existing WFD hardware and unattractive to use because of the significant hadronic flash, which added a large and slowly decaying baseline for many of the detectors in the first half of the ring. Our new digitizers will be capable of storing all the samples from a complete fill so Q -method running can be enabled as a parallel data stream; the lack of a hadronic flash should keep the pedestal baseline relatively flat.

B. Electromagnetic Calorimeters

1. The E821 calorimeters

The 24 E821 electromagnetic calorimeters are made of plastic scintillating fibers epoxied into a grooved lead alloy plate. The material ratio is 52:38:10 lead:scintillator:epoxy, which gives a 1.15 cm radiation length (X_0) and a 2.5 cm Moliere radius (ρ_M). The compact 15 cm depth avoids a high fraction of side-entering positrons. The system is described in

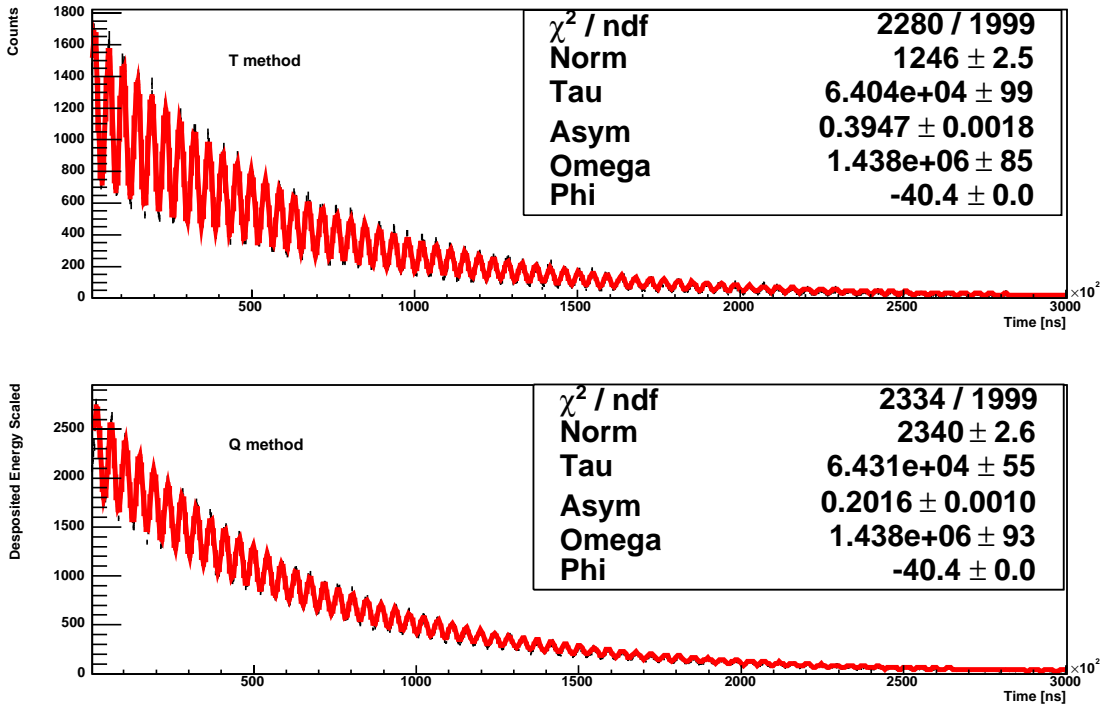


FIG. 16: GEANT simulation of events. Upper panel: Data analyzed using the tradition T method with $E_{th} = 1.8$ GeV. Lower panel: Data prepared using Q method, representing energy vs. time. Note the poor χ^2/dof for each plot is because the fits were performed using a simple 5-parameter function, which ignores the coherent betatron oscillations present in the simulation.

detail in Ref. [18]. The calorimeter stations are placed symmetrically around the inside of the storage ring immediately adjacent to the vacuum chamber, which has a scalloped shape to permit decay positrons to exit a flat face cutout just upstream of each calorimeter. The radially-oriented fiber grid terminates on four lightguides that pipe the light to independent Hamamatsu R1828 2-inch PMTs. The PMT gains are carefully balanced because the four analog signals are added prior to sampling by the waveform digitizer. The fractional energy resolution is approximately 7.0% at 1.9 GeV and scales as $1/\sqrt{E}$. While initial calibration and quadrant balancing was performed at the BNL test beam, very precise calibration information is determined *in situ* from the positron energy spectra. The final calibration was performed by collecting data for each of the four quadrants separately. Because of the hadronic flash, all PMTs are gated off prior to injection and are turned back on some tens of microseconds later, depending on the location around the ring. The switching circuit

reverses the bias on dynodes #4 and #7 of the PMT base, thereby effectively truncating the cascade in midstream. The dynodes can be reset to their normal configuration and the gain of the PMT re-established to better than 99 percent of its steady-state value in approximately 1 μ s.

A 300 ps UV (337 nm) pulse from a nitrogen laser is directed through a splitter system into the outside radial end of each of the quadrants of all calorimeters. The UV pulse is absorbed by a sample of scintillating fibers and is re-emitted following the scintillating fiber fluorescence spectrum. This signal propagates through the entire optical system, with a digital readout identical to that produced by an ordinary positron shower. A reference photodiode and PMT—located away from the beam—also receive a fixed fraction of the light from the laser pulse. The system is capable of establishing limits on timing shifts of less than 2 ps; however, gain stability measurements suffer because the current system is not stable in the ratio of light conveyed to the reference detectors and to the calorimeters at a level better than about 1 percent. The limitation of accuracy in the gain-stability determination is in the calibration system, not the detectors. The detectors have a gain stability of a few tenths of a percent, determined by direct inspection of the average energy spectrum vs. time. This instability of the calibration system must be corrected to achieve the accuracy required in this new proposal

2. New segmented calorimeters for P969

In the new experiment, the PMT switching circuit can be avoided because the hadronic flash will be absent. This change will leave the PMTs at a constant voltage; we believe small shifts in the gain vs. time are related to the switching circuit. If a modest suppression of positrons is required, an alternate method is to pulse a grid on the front face of the PMT, obtaining without difficulty a suppression of about 100 (the E821 suppression was 10^6). The calibration system must be re-designed to guarantee internal stability in the ratio of light distribution. The concept worked quite well with laser pulses injected during special runs, roughly once per shift. However, the implementation was not as robust as required for our data analysis demands. This can be improved by having local reference detectors at each calorimeter station. For the PSI experiments, we are using a new LED system to maintain calibration; we can adopt this system if it performs at the 0.1 percent level or better.

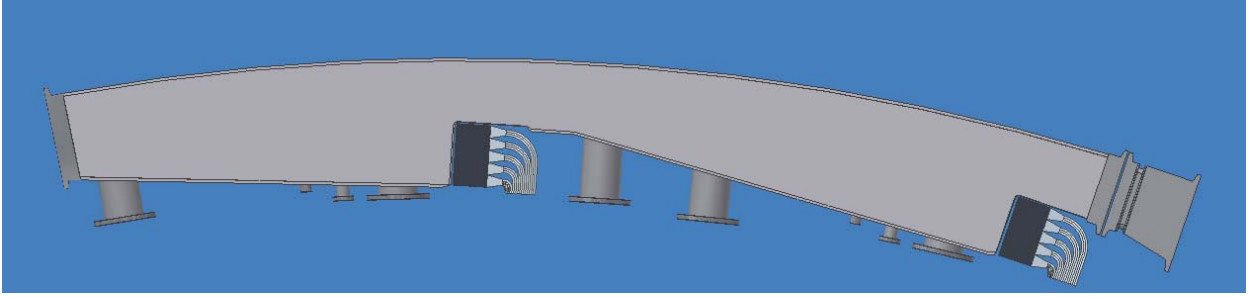


FIG. 17: Plan view of new calorimeters and existing scalloped vacuum chamber region.

The basic material design requirements for a new calorimeter are largely unchanged; it must be dense and fast. Additionally, the new calorimeter must be segmented transversely with respect to the incoming positron so that simultaneous events can be distinguished. We estimate that recognizing simultaneous events 4 out of 5 times is necessary to accommodate the fivefold increase in positron decay rate, while keeping the uncorrected pileup fraction at the same level as in E821.

Appendix D includes a more detailed description of a tungsten / scintillating fiber (W-SciFi) sampling calorimeter that meets these demands. Briefly, it

- is made of alternating flat plates of tungsten and ribbons of scintillating fiber, giving $X_0 = 0.7$ cm and $\rho_M \approx 1.7$ cm;
- has 20 independent segments read out by individual PMTs located outside of the field region;
- has a resolution of about 10 percent at 2 GeV, when using layer thicknesses of 0.8 mm; and
- uses standard 29 mm PMTs having high-rate bases.

The design plans are preliminary and we expect to study variants on this basic design and then build one or more prototypes in the near future. It is important that the detector fit within constraints of the ring instrumentation, which protrudes from the vacuum chambers to accommodate different instrumentation. A plan view of the vacuum chamber and the detector positioning is shown in Fig. 17, indicating that this design looks promising for the standard vacuum chamber sections.

C. New front scintillator hodoscope—FSH

Each of the present calorimeters is outfitted with a five-fold, vertically segmented scintillator hodoscope—front scintillating detectors (FSD). The FSDs were used to determine the time-dependent rate of “lost muons” from the storage ring and to give a coarse vertical profile of positrons on the front face of the calorimeters. The muon loss signal is made from three consecutive FSD stations in coincidence; lost 3.1 GeV muons penetrate three calorimeters with a probability of about 5 percent. FSD vertical profiles were used to measure the average height of muons in the storage ring; the height was then centered by adjusting the radial field. Because of deadtime in the FSD readout electronics and the intrinsic coarse segmentation, the FSDs were not used for pileup rejection.

A proposed new front scintillator hodoscope (FSH) will consist of 10 horizontal scintillator strips having variable widths inversely proportional to the average rate in each vertical band. The scintillators will be coupled by a nearly straight acrylic rod to a small PMT. The strips will define a fiducial entrance window on the face of the calorimeter leaving a 1 cm uncovered “border” at the top and bottom. The light will be piped to 19-mm (3/4-in) PMTs located about 1 m away radially. The demands on the PMTs are similar to those for the calorimeter. An appropriate choice is the Photonis XP-1910. We expect to use standard leading-edge, updating discriminators having ECL outputs. The discriminated signals will be digitized using a multi-hit TDC, an example of which is being employed in our PSI experiments. Additionally, the analog sum signal from the ten PMTs will be digitized by an additional WFD channel. That signal will provide additional information that can be used in a pileup-rejection scheme.

D. Waveform digitizers

We are building 100, four-channel, 500 MHz waveform digitizers for our two precision muon lifetime experiments at PSI. These modules are conceptually very similar to those used by us in E821, however, there are several important improvements. First the signal is sampled by an 8 bit, 500 MHz flash ADC (FADC). The output of the FADC is sent to a field programmable gate array (FPGA), where the data is reformatted, given a time stamp, and exported to an external first in-first out (FIFO) memory. The modules sit in a VME-64x

crate (slightly modified to provide a few non-standard voltages). Data from each of the modules in a given crate is readout with a Struck PCI-VME interface card at rates up to 80 MB/s. Unlike the E821 WFD, the dual port FIFOs allow the events to be read out while data taking continues. Not only does the new WFD have more onboard memory, faster sampling, and higher readout speed, it is also far more flexible than the old E821 WFD. By reprogramming the FPGA we can reformat the output data as desired. Indeed, we have defined a number of "personalities" for the board, each of which can be programmed through a JTAG interface, to match the needs of the particular data stream. For example, the T and Q methods will each use WFDs that prepare the process and store the data differently.

The full bank of waveform digitizer modules is scheduled to be delivered and used for the 2005 physics production runs at PSI. We anticipate two years of operation there to complete those experiments. After that, the WFDs will be free to be used for P969. An additional 150 channels will have to be built for P969.

In parallel with this development, our Collaboration has written the custom software to readout the new WFDs and is preparing the on-the-fly pulse-fitting software (see DAQ section below). In the PSI MuLan experiment—for which the WFDs were developed—more than 2×10^{12} events will be recorded. In the new ($g - 2$) experiment the number of events is lower by a factor of 20 while the number of samples to be recorded is higher by about a factor of 3. Thus, the two efforts are roughly similar in data-flow and processing requirements. Our team will have great experience with the use of the new WFDs and their readout and interpretation.

A time base having 0.01 ppm accuracy and stability over months is not difficult to obtain; vendors such as Precision Test Systems and Agilent can provide synthesizers driven by ovenized oscillators, which meet that specification. For the MuLan experiment in the fall of 2003, the system clock was generated with an Agilent E4400 synthesizer. The (approximately) 200 MHz system clock was mixed with another roughly 200 MHz signal from a PTS 3100 (which was previously used to drive our E821 clocks). This difference frequency was stable at 0.5 Hz over several weeks of operation. We also measured the outputs of the Agilent and PTS clock signals with a recently calibrated and highly stable frequency counter. The Agilent signal was absolutely accurate to 0.01 ppm while the PTS signal was 0.1 ppm too high. During the course of operation, no systematic frequency drift was observed on either clock. When tested again nine months later, the Agilent clock signal drifted by no

more than 30 ppb. The same system clock frequency is delivered to the NMR system and to the electronics that determine the ω_a frequency so only the relative stability is important.

We have already built a clock distribution system to fan out clock signals to the WFDs. This system is based on linear fanouts used in E821 and other precision experiments. The 500 MHz system clock is sent as input to a 1-to-8 splitter/amplifier module and then by six 1-to-16 splitter/amplifier modules. The remaining two copies from the 1-to-8 splitter module are used to drive a frequency tracking system and a clock divider module. Frequency tracking during the experiment is done either with a calibrated frequency counter or a mixer system like that discussed above. An additional modular subsystem performs clock division duties by means of ECLips logic circuits: various modules can be connected to produce square wave clock signals at integer submultiples of the system clock frequency, and in a variety of logic levels (ECL, LVTTTL, etc). These derived square wave clocks are used, for instance, to drive flight simulator and multi-hit TDC hardware.

E. Data Acquisition

In the E821 data, only the summed signal from the four calorimeter segments was recorded in a WFD, and only pulses with energies greater than approximately 1 GeV were stored, together with a number of samples in their vicinity. Ideally, to reduce the systematic uncertainty from overlapping pulses, every sample from each segment would be recorded with no threshold; then the full energy distribution could be measured as a function of time with maximum segmentation. Unfortunately, it is not practical to acquire and store this much data. Instead, as a compromise, the readout scheme will be improved in two complementary ways:

- Each of the 20 segments of the new calorimeters will be recorded in a separate WFD channel, rather than only storing their sum. These data would be used for the “standard” T method analysis.
- The sum of the segments will also be recorded in a WFD with a different “personality” in which no zero suppression is performed. All samples from each 600 μ s fill will be recorded in an unbiased way, but only for the sum. These waveforms may be used for the Q method analysis or for an alternate T method analysis.

There will be five WFD boards for each calorimeter, each with four channels, to provide the segmented readout. The threshold will be set, as it was in E821, to correspond to a 1 GeV positron pulse. To ensure that the threshold remains constant regardless of the sharing of the energy of the shower among segments, it will be applied to the summed signal across all segments. The analog signals from all twenty segments will pass through a signal conditioning board (SCB), which will construct and discriminate their sum. While all of the WFDs in the segmented readout will always be triggered together, “blank” waveforms from parts of the calorimeter that were not hit will be filtered out by the frontend software to reduce the data rate. In each fill, we may expect to record approximately 500 pulses per detector with energies greater than 1 GeV, storing approximately 32 ADC samples per segment, and with an average occupancy of about 6.5 segments. There will be twelve fills per 2.6 s AGS cycle. Consequently, the contribution to the data rate from the segmented approach may be expected to be about 12 MB/s.

The summed output from the SCB will also be sent to a dedicated WFD channel. The FPGA “personality” of this WFD will not employ zero suppression, but it will use an algorithm based on standard lossless techniques such as run-length encoding and Huffman coding [61] to compress the summed waveforms. The duration of each fill will be approximately 600 μ s, so there will be 3×10^5 samples per detector per fill. Consequently, the raw data rate before compression will be 33 MB/s. Experience with similar problems suggests that a factor of 3 to 5 reduction in data volume may be expected from lossless compression of this data, reducing it to at most 11 MB/s. We note that it would also be possible to simply rebin the ADC samples into 20 ns bins to reduce the data rate by a factor of 10 without the use of compression algorithms. The resulting spectrum could still be used in the Q method, but would not provide enough resolution to use in an alternate T method analysis.

The total data flow rate is then expected to be 23 MB/s; it may be somewhat lower if the online compression is more effective, or slightly higher if more muons per fill are stored. It is anticipated that there will be twelve VME crates; they will be located in the experimental hall, adjacent to the detectors. Each will serve a pair of detectors, so the overall rate in each will only be 2 MB/s. The instantaneous rate in each crate during the extraction part of the AGS cycle will be 14 MB/s, so it should easily be possible to completely empty each FIFO memory between fills. The crates will be connected through industry-standard

gigabit Ethernet links to an event-builder PC, which will write the data to an LTO-2 tape drive. LTO-2 tapes hold 200 GB per tape without compression, and they may be written and read at speeds of up to 35 MB/s. A subset of the data will also be saved on a local disk array for online and fast-turnaround offline analysis. If we collect data for the entire proposed 1800 hour run at the projected 23 MB/s, we will amass 150 TB of raw data, filling 750 tapes.

The data acquisition software to be used with the new WFDs will be based on our experience in the MuLan and MuCap experiments at PSI. It will use MIDAS [64], which provides a framework for network data transfer, event building, logging to tape or disk, run control, and both online and offline analysis.

MIDAS also permits slow control and monitoring data to be integrated with the fast data stream for easy correlation. In addition, it has a mechanism for making history plots and setting alarms based on the slow control data. A web browser interface is typically used to view and set slow parameters, but it is also possible to interact with them programmatically and from scripts. We intend to use these capabilities to bring together the readout from many of our subsystems.

The “production,” or first-level reduction, of the data will require significant computational resources, as will subsequent phases of the analysis. The core of the data analysis system will be a computer farm built of 60 dual-CPU computers, each with a significant amount of disk storage. The farm will be used for the production of the raw data, for user analysis of the produced data, and as a distributed disk array. We aim to keep all of the produced data on disk, which will require about 30 TB of disk space. Each node of the farm will house 0.5 TB, setting the total number of nodes required at 60. Such a farm should allow us to produce all of the expected data within one month and to loop over all produced data within one day.

F. Systematic uncertainties on ω_a

The largest systematic uncertainties in the 2001 ω_a analysis give a quadrature-combined total of 0.19 ppm (we assume these are uncorrelated uncertainties)[71] Our goal is a factor of two reduction, to ≈ 0.1 ppm. We believe we can meet this goal by enlisting a suite of improvements to the experiment. Here, we address in detail the plan to reduce the

largest sources of systematic error: gain changes, lost muons, pileup and coherent betatron oscillations; the 0.05 ppm systematic uncertainty associated with the electric field and pitch correction remains unchanged (for now). Table V lists these uncertainties and projections for improvements. The T method is assumed because uncertainties can be reliably projected based on our considerable experience in the E821 analysis efforts. The Q method, on the other hand, is new. Its most attractive feature is pileup immunity; there is no correction necessary so that systematic uncertainty is absent. However, new Q -specific systematic issues may arise (we know of none at this time), and we continue to study this method before venturing to make a meaningful projection of expected systematic uncertainties.

1. *Gain changes and energy-scale stability*

Typically, the gains of the detectors were determined to be better than $\approx 0.15\%$ from early to late times. This limit was established by plotting the average energy in a detector—over a full $(g - 2)$ cycle—versus time after the PMTs were switched on. For a slowly varying gain compared to the $(g - 2)$ oscillation period having no component that oscillates at frequency ω_a , then a gain shift at this level does not contribute significantly to the uncertainty in ω_a .

On the other hand, if the gain oscillates at a frequency ω_a , with an amplitude that varies in time, and with a phase that differs from that of the ω_a oscillation of the positron sample, then a direct error on ω_a is produced. The average rate at which energy deposited into the calorimeters oscillates with frequency ω_a , and therefore any rate dependence in the gain of the detectors produces gain oscillations. We were able to demonstrate that the gain dependence on rate was small enough that its effect on ω_a was typically less than 0.03 ppm. In the new experiment, the increased beam rates will be offset by increased detector segmentation, and we expect this effect of rate-dependent gain to remain unchanged.

By far the greatest contribution to the gain systematic error came from artificial gain oscillations at the ω_a frequency, introduced by the data reconstruction software. Whereas “gain” implies a hardware response, the “energy-scale” stability is related to software reconstruction of waveforms. We give separate entries for these items in Table V. When a signal was above the hardware threshold level, indicating the arrival of a high-energy positron, a pre-arranged minimum number of sequential WFD samples, sufficient to cover the pulse, were transmitted from the WFD to data storage. These data were fit offline for the peak

plus linear background to deduce the energy and time of the positron. If the pulse that triggered the WFD readout is followed closely by another pulse, then the two peaks are fit together with a common background term, and the fitting region is longer than for a single peak. The energy of the positrons was found to depend slightly on the length of the fitting region. Noting that the data rate oscillates at frequency ω_a , and is higher at early than at late decay times, it follows that the fitting region length will oscillate at ω_a and it will be on average longer at early times than at late times. This produces a small gain oscillation with frequency ω_a whose amplitude decreases with time, leading to a systematic error on ω_a . We expect to simulate this effect in detail and reduce its effect in the new experiment by a factor of three. The reduced flash will lead to improved data fitting, making such studies much easier than would have been the case in the past. Additionally, our Q -method data set will contain all samples, meaning a stream of unbroken islands from which detailed systematic studies can be made in the event that a correction is necessary due to island length correlation. We estimate a residual uncertainty in the overall gain and energy of less than 0.03 ppm.

2. *Lost muons*

“Lost muons” refers to muons that escape the storage ring before they decay. These losses are about 1% per lifetime at early decay times and decrease to about 0.1% at later decay times. One consequence of losses is that, in a fit to the data, the lifetime is not quite correct. This is a slow change in the spectrum with time, having no ω_a frequency component; therefore the contribution to the error in ω_a is negligible.

The stated error in Table V from muon losses comes mainly from the uncertainty in the difference between the average phases for stored and lost muons. For example, one source of muons, carrying a different phase and potentially lost at a higher rate, are those created after the momentum-selecting slit just upstream of the inflector. These muons, born from pion decay in that short region, have a different phase compared to those captured in the FODO decay channel (the later muons did not go through the final dipole bend, which precesses the muon spin). Muons born in the FODO section at large angles carry a different phase compared to those having a smaller initial angles. If they are lost preferentially early in the spill, the ensemble muon population phase also shifts. In the new beam method, all

muons will be captured in the FODO section and thus all will carry the same initial phase. Additional quads should improve containment.

Nevertheless, we do not know with certainty which muons are lost, and therefore we are forced to make a worst-case estimate of the maximum possible phase shift, which we continue to do here. We plan to reduce losses by a factor of at least two, thereby reducing the contribution to ω_a error by a corresponding factor. This will be achieved by increasing the scraping of the beam—see Appendix B—at the expense of stored beam flux. We therefore project an uncertainty of approximately 0.04 ppm. In addition to improved scraping, we plan to do more extensive spin-tracking simulations of the beamline from the FODO section directly into the storage ring. At the level of uncertainty associated with the statistics of E821, this full effort was not warranted; we used an extreme upper limit from simple Monte Carlo instead. For P969, we will carry out these simulations, which will permit a better limit to be established regardless of the level of muon loss.

3. *Pileup*

The error due to pileup scales linearly with rate in each segment of the detectors. The effective size of the segment depends on the geometric extent of the shower. The improved tungsten-plate detector system, with more segments and smaller Moliere radius than the previous Pb/SciFi detectors, provides an effective five-fold reduction in pileup. With no further improvements, and with the proposed factor of 5 increase in data rate, the pileup error would remain at the 2001 level of 0.08 ppm. While we could accept this level of error, some improvement is desirable and achievable.

In the past, in order to reduce the effect of pileup in fits to the time spectrum of positrons, a pileup spectrum was constructed from individual pulses in the data, then subtracted from the raw spectrum. In the pileup construction, it is necessary to use pulses with pulse heights below as well as above the hardware threshold. Those pulses below threshold are only found by searching during the relatively short period of continuous WFD digitization following the trigger generated by the presence of a large pulse above threshold; this leads to limitations on the size of the sample of pulses below threshold available for pileup reconstruction and can also lead to a slight bias of the pulses since they always follow on the tails of larger pulses. In the new data acquisition scheme, it will be possible to significantly improve the

pileup construction process. Continuous digitization, with local software pulse finding, is anticipated. Pulses of all heights can be searched for independent of whether there is a nearby large pulse that fired a hardware trigger; furthermore, in the absence of a flash, it will be possible to find and include smaller pulses in the pileup construction.

In the previous ($g - 2$) experiment, signals from four detector segments were combined before WFD digitization. Any mismatch in the relative timing of these signals can lead to variation in the pulse shape of the sum. In addition, the scintillator fiber in the calorimeters was strung radially, causing the pulse shape to depend slightly on the radial entrance position into the detector. These variations in the pulse shape hampered efforts to handle pileup, both in the fitting of two nearby peaks, and in the process of constructing the pileup spectrum. The pulse shape is expected to be more stable in the new design, because each segment will be individually digitized, the scintillator will be oriented azimuthally, and special efforts will be made to reduce reflections in the calorimeter scintillator, which can widen the pulses in a position-dependent way.

The contribution of pileup to the error in ω_a can be divided into three components. The first two are correlated and add linearly. The third is not correlated so it is added in quadrature to the other two, arriving at a new quoted uncertainty of 0.08 ppm for our 2001 analysis.

1. Pileup efficiency, 0.036 ppm. This is due to an estimated 8% uncertainty in the amplitude of the constructed pileup spectrum.
2. Pileup phase, 0.038 ppm. This is the error due to the uncertainty in the phase of the constructed pileup spectrum.
3. Unseen pileup, 0.026 ppm. This is the error due to pulses so small that they cannot be reconstructed and therefore they are not included in the pileup construction. With the reduced flash background, we expect to be able to see smaller pulses than before, with improved fit quality. We will also have the advantage that in our Q -method data taking, the complete sample of data will be accumulated with no hardware threshold.

We believe that the unseen pileup uncertainty will be reduced by a factor of 2. The pileup efficiency and phase uncertainty will be lowered slightly because of the much more complete data stream, which extends to zero energy. The efficiency in particular will be lower because

of the inclusion of the highly segmented FSH detector system. However, without extensive study, we do not yet project these improvements much beyond the current status. We use an uncertainty of 0.07 ppm as our estimate.

The Q method is complementary to the traditional T method and has different sources of systematic errors. The most significant difference is the effect of pileup—it vanishes for the Q method.

4. Coherent Betatron Oscillations

The average position and width of the stored beam can vary as a function of time as the beam alternately focuses and defocuses in the ring. This imposes an additional time structure on the decay time spectrum because the acceptance of the detectors depends on the position and width.

It happens that one of the beat frequencies associated with the horizontal CBO is near ω_a , causing interference with the data fitting procedure and leading to a systematic error. For the 2001 data-taking period, we choose the electrostatic focusing strength, characterized by the field index n , such that the CBO beat frequencies was as far as possible from ω_a . This greatly reduced the CBO systematic uncertainty from the 2000 analysis. We will follow this tuning strategy again.

In addition, several efforts are underway to reduce the CBO effect even further. They include:

1. Use active rf schemes at very early decay times to reduce the amplitude of the CBO (see Appendix B),
2. Use an octupole E or B field at very early decay times to damp out the CBO amplitude (see Appendix B),
3. Increase the vertical size of the detectors. This reduces losses of positrons passing above or below the detector, reducing sensitivity of the detector acceptance to beam position and width.

The combined efforts should reduce the CBO uncertainty by a factor of 2 to 0.04 ppm.

5. Electric field and pitch correction

With a vertical magnetic field B_y and radial electric field E_r , the precession frequency is given by

$$\omega_a = -(e/m)[a_\mu B_y - (a_\mu - 1/(\gamma^2 - 1))\beta E_r]. \quad (24)$$

If B_y and E_r vary with position, the time averages $\langle B_y \rangle$ and $\langle E_r \rangle$ should be used. At exactly the magic momentum the effect from E_r is zero. Muons of slightly higher momentum δp have an equilibrium orbit

$$x_e = \frac{R_o}{1-n} \cdot \frac{\delta p}{p}.$$

As they oscillate about this equilibrium orbit they experience a mean electric field $\langle E_r \rangle = n(\beta B_y/R_o) x_e$ and their deviation from the magic momentum is proportional to x_e . This leads to a correction to ω_a proportional to x_e^2 . In this experiment n is measured from the observed horizontal betatron frequency, and the distribution of muons with respect to x_e is found from the modulation of counting rate by the rotation frequency of the muon bunch. The observed value of $\langle x_e^2 \rangle$ was confirmed by simulation. The correction is 0.46 ppm.

With electric focusing, the plane in which the muon spin is precessing oscillates vertically, exactly following the oscillation of the muon momentum. When the orbit is inclined at angle ψ to the horizontal, ω_a is reduced by the factor $(1 - \frac{1}{2}\psi^2)$. If ψ_m is the angular amplitude of the vertical oscillation, the average over the ensemble of muons is $(1 - \frac{1}{4}\langle \psi_m^2 \rangle)$ where the brackets indicate an average over the muon population, $\langle \psi_m^2 \rangle = n\langle y_m^2 \rangle/r_o^2$ where y_m is the amplitude of the vertical oscillation.

Information on $\langle \psi^2 \rangle$ is obtained by simulation in which a representative set of muons is tracked round the ring from the inflector exit, via the kicker magnet, for many turns. The discrete quadrupole structure and aperture defining collimators are included as well as the calculated deviations from a pure quadrupole field. The pitch correction is +0.29 ppm.

A combined (correlated) electric field and pitch correction uncertainty of 0.05 ppm was used in E821 and we adopt that number for our future estimates.

6. ω_a systematic uncertainty summary

Our plan of data taking and hardware changes address the largest systematic uncertainties and keeps their combined total at approximately 0.11 ppm, which, at this level of projection,

TABLE V: The largest systematic uncertainties for the 2001 ω_a analysis and proposed upgrade actions and projected future uncertainties for data analyzed using the T method.

E821 Error	Size	Upgrade Plan	Goal
	[ppm]		[ppm]
Gain changes	0.12	Gain: unchanged	0.03
		Scale: pulse shape, island length immunity	0.03
Lost muons	0.09	New scraping to reduce losses	0.04
Pileup	0.08	Low-energy samples recorded; segmentation	0.07
CBO	0.07	New scraping / taller calorimeters	0.04
E and pitch	0.05	Remains the same	0.05
Total	0.18	Quadrature sum	0.11

is certainly within our error allotment for ω_a . Experience shows that many of the “known” systematic uncertainties can be addressed in advance and minimized, while other more subtle uncertainties appear only when the data is being analyzed. Because we have devised a method to take more complete and complementary data sets, we anticipate the availability of more tools to diagnose such mysteries should they arise. Table V summarizes this section.

VIII. MANPOWER

We have formed a new collaboration to carry out this measurement. Fortunately, much of the expertise built up in E821 is represented and still available to us. We still have senior experts in the collaboration who cover all of the different technical areas. New institutions have also joined the effort including UC-Berkeley and Lawrence Berkeley Laboratory, James Madison University, and the University of Kentucky. Several other groups are interested in participating and we expect them to sign on once the project timeline is better defined. As the experiment develops, we expect additional postdocs and students to sign on. We are proud that E821 offered a rewarding experience for dozens of postdocs and graduate students and we intend to welcome young physicists in the new effort.

IX. RESOURCES AND COSTS

While we have developed substantial expertise in our collaboration on beamline related issues, the final design of the new 5.3 GeV/ c front end of the beamline and the cost to add more quadrupoles to the FODO section will require input by the Laboratory. Obviously the construction and installation of the new elements will fall under the Laboratory's responsibility, aided by the Collaboration.

As before, we will need the support of the CAD Cryogenics group for the operation of our magnet.

The superconducting inflector will need to be fabricated, either at BNL, or in Japan, if our Japanese colleagues are interested in building the revised inflector.

One of the issues in the precision field is the lack of temperature control in the hall. Temperature changes cause the yoke to expand or contract, changing the magnet gap and the field. For E821 we wrapped the magnet in thermal insulation which reduced the sensitivity to temperature changes in the hall. In the new experiment we will need to temperature control the hall to improve the magnetic stability of the storage ring. A design was prepared for E821, but was never implemented.

We assume that the detectors, electronics, and data acquisition system can be obtained from our individual funding agencies through the university program and a supplemental grant. Most of the custom waveform digitizers needed for this experiment will be available

from the MuLan effort, once that experiment is complete. We expect the total cost of the detectors, electronics and DAQ to be close to \$1M.

X. TIMESCALE

While scientific approval with highest priority is necessary for us to go forward, it is only the first step in realizing the goals of this proposal. When we visited the Department of Energy in March 2004, we were told by the Director of the Office of High Energy Physics to proceed through the usual proposal process at the Laboratory. If this approval is granted, then we will need to join with the Laboratory to go back to the agency to obtain support to carry out this new experiment. While we cannot know the timescale on obtaining the necessary funding, for the sake of this discussion we will assume that it will take on the order of one year from approval, or roughly the beginning of FY06.

Once funding is obtained, we believe that it will take two years for the construction of the new beamline, the new inflector, along with the new detectors and other hardware.

The storage ring magnet would need to be powered for shimming and tests for a substantial period of time before any running could occur. One possibility would be to cool the magnet in early FY08, with the period of pulse on demand, followed by a three-week engineering run in the late spring of 2008. The major data run could then take place in FY2009.

XI. SUMMARY OF THE REQUEST

We propose to improve the E821 measurement of a_μ by a factor of 2.5. Combined with progress on the theoretical value, a 0.2 ppm result can more than double the sensitivity of the measurement to standard model extensions. The hint of standard model violation in the final E821 result may be contradicted, or verified, but whether the new result agrees with the standard model or not, it will place important constraints on models of new physics.

In this proposal, we have identified a timely and cost-effective extension of the E821 measurement, which makes maximum use of the investment to date in the Brookhaven muon storage ring and related apparatus. It is a task well matched to our expertise and one that will provide unique insight into fundamental questions in high-energy physics.

-
- [1] An overview of non-standard model physics is given by T. Kinoshita and W.J. Marciano in *Quantum Electrodynamics* (Directions in High Energy Physics, Vol. 7), ed. T. Kinoshita, (World Scientific, Singapore, 1990), p. 419.
- [2] M. Davier and W.J. Marciano, *Ann. Rev.* in press, (2004).
- [3] G.W. Bennett, et al., (Muon ($g-2$) Collaboration), *Phys. Rev. Lett.* **92**, 161802 (2004). Spires shows that this paper has 35 citations.
- [4] R.S. Van Dyck et al., *Phys. Rev. Lett.*, **59**, 26(1987) and in *Quantum Electrodynamics*, (Directions in High Energy Physics Vol. 7) T. Kinoshita ed., World Scientific, 1990, p.322.
- [5] T. Kinoshita, *Rep. Prog. Phys.***59**,1459 (1996) which is updated in T. Kinoshita and M. Nio, *Phys. Rev. Lett.* **90**, 021803-1.
- [6] R.M. Carey et al., *Phys. Rev. Lett.* **82**, 1632 (1999).
- [7] H.N. Brown et al., (Muon ($g-2$) Collaboration), *Phys. Rev.* **D62**, 091101 (2000).
- [8] H.N. Brown, et al., (Muon ($g-2$) Collaboration), *Phys. Rev. Lett.* **86** 2227 (2001). Spires shows that this paper has 483 citations.
- [9] G.W. Bennett, et al., (Muon ($g-2$) Collaboration), *Phys. Rev. Lett.* **89**, 101804 (2002). Spires shows that this paper has 233 citations.
- [10] F. Krienen, D. Loomba and W. Meng, *Nucl. Inst. and Meth.* **A 283**, 5 (1989).
- [11] A. Yamamoto, et al., *Nucl. Instrum. and Methods Phys. Res.* **A491** 23-40 (2002).
- [12] G.T. Danby, et al., *Nucl. Instr. and Methods Phys. Res.* **A 457**, 151-174 (2001).
- [13] Efstratios Efstathiadis, et al., *Nucl. Inst. and Methods Phys. Res.* **A496** ,8-25 (2002).
- [14] Y.K. Semertzidis, *Nucl. Instrum. Methods Phys. Res.* **A503** 458-484 (2003)
- [15] S.I. Redin, et al., *Nucl. Instrum. Methods Phys. Res.* **A473**, 260-268, (2001).
- [16] R. Prigl, et al., *Nucl. Inst. Methods Phys. Res.* **A374** 118 (1996).
- [17] X. Fei, V. Hughes and R. Prigl, *Nucl. Inst. Methods Phys. Res.* **A394**, 349 (1997).
- [18] S.A. Sedykh et al., *Nucl. Inst. Methods Phys. Res.* **A455** 346 (2000)
- [19] J. Ouyang et al., *Nucl. Instrum. Methods Phys. Res.* **A374**, 215 (1996).
- [20] D.W. Hertzog et al., *Nucl. Instrum. Methods Phys. Res.* **A294**, 446 (1990).
- [21] J. Bailey et al., *Nucl. Phys.* **B150**, 1 (1979).
- [22] T. Kinoshita and M. Nio, *Phys.Rev.Lett.*90:021803,2003, and Toichiro Kinoshita and M. Nio,

- arXiv hep-ph/0402206, Feb 2004.
- [23] A. Czarnecki, B. Krause and W.J. Marciano, Phys. Rev. Lett. **76** (1996) 3267.
 - [24] R.R. Akhmetshin, et al, CMD2 collaboration, Phys. Lett. **B 527**, 161 (2002).
 - [25] R.R. Akhmetshin, et al, CMD2 collaboration Phys. Lett. **B578** 285 (2004).
 - [26] M. Davier, S. Eidelman, A. Höcker, and Z. Zhang, Eur. Phys J. **C 27** 497 (2003). See K. Hagiwara, A.D. Martin, D. Nomura, and T. Teubner Phys. Lett. **B557**, 69 (2003) for an independent analysis of the e^+e^- data.
 - [27] M. Davier, S. Eidelman, A. Höcker, and Z. Zhang, Eur. Phys. J. **C 31**, 503 (2003).
 - [28] A. Aloisio, et al., (KLOE Collaboration) arXiv hep-ex/0407048, July 2004 and submitted to Phys. Lett.
 - [29] Federico Nguyen, daφne workshop, Frascati, June 2004, <http://www.lnf.infn.it/conference/2004/dafne04/> and Juliet Lee-Franzini, private communication, July 2004.
 - [30] R. Alemany, M. Davier and A. Höcker, Eur.Phys.J. **C2** 123 (1998).
 - [31] M. Davier and A. Höcker, Phys. Lett.**B435**, 427 (1998).
 - [32] Y. Orlov, C.S. Özben and Y.K. Semertzidis, Nucl. Instrum. Meth. **A482**, 767 (2002).
 - [33] S. Ghozzi and F. Jegerlehner, Phys. Lett. B 583, 222 (2004).
 - [34] M. Davier, SIGHAD2003, arXiv hep-ex/0312065, (2003)
 - [35] W. Marciano, Private communication, 2004.
 - [36] A. Aloisio, et al., Phys. Lett. **B561**, 55 (2003).
 - [37] Kirill Melnikov, at From Zero to Z^0 , FNAL 13 May 2004 and private communication.
 - [38] Marc Knecht, Andreas Nyffeler, Phys. Rev. **D65**, 073034 (2002); M. Knecht, A. Nyffeler, M. Perrottet, E. De Rafael, Phys. Rev. Lett. **88**, 071802 (2002), J. Bijnens, E. Pallante, and J. Prades, Nucl. Phys. **B626**, 410 (2002); M. Hayakawa and T. Kinoshita arXiv hep-ph/0112102, (2002), I. Blokland, A. Czarnecki and K. Melnikov Phys. Rev. Lett. **88**, 071803 (2002).
 - [39] K. Melnikov and A. Vainshtein, arXiv hep-ph/0312226, 2003.
 - [40] Andrzej Czarnecki and William J. Marciano, Phys. Rev. **D64** 013014 (2001).
 - [41] Juliet Lee-Franzini, private communication, July 2004.
 - [42] Vera Luth, private communication, June 2004.
 - [43] Steve Dytman, private communication, July 2004.
 - [44] Simon Eidelman, private communication, July 2004.

- [45] T. Blum, Phys. Rev. Lett. **91**, 052001-1 (2003).
- [46] T. Blum, Nucl. Phys. Proc. Suppl. **129**, 904-906,2004, and arXiv hep-lat/0310064,
- [47] T. Blum, private communication, July 2004.
- [48] Keh-Fei Liu, private communication, July 2004.
- [49] E. Eichten, et al., Phys. Rev. Lett. **45**, 225 (1980), K. Lane, arXiv hep-ph/0102131, 2001.
- [50] Particle Data Group, Phys. Lett. **592** 340 (2004)
- [51] The articles listed in the SPIRES citations to Ref. [8] contain many different models beyond the standard model.
- [52] U.Rohrer, PSI GRAPHIC TRANSPORT FRAMEWORK and PSI GRAPHIC TURTLE FRAMEWORK based on the CERN-SLAC-FERMILAB TRANSPORT and DECAY TURTLE by K.L. Brown et al. CERN 80-04 (1980) and SLAC-246 (1982).
- [53] W. Liu et al., Phys. Rev. Lett. **82**, 711 (1999).
- [54] BNL E821 Design Report, 3rd Edition (B.L. Roberts editor) March 1995.
- [55] R. Prigl, PhD Thesis, U. Heidelberg (1994).
- [56] A.P. Grossmann, PhD Thesis, U. Heidelberg (1998).
- [57] S.I. Redin, PhD Thesis, Yale University (1999).
- [58] H. Deng, PhD Thesis, Yale University (2002).
- [59] Superintendent of Documents, *LORAN-C User's Handbook*, U.S. Government Printing Office #050-012-00331-9, 1992.
- [60] P. Neumayer, Diploma Thesis, U. Heidelberg (1999), and references therein.
- [61] D. A. Huffman, *Proceedings of the Institute of Radio Engineers* **40** 1098 (1952); see also *Numerical Recipes* section 20.4 and references therein.
- [62] Paul Scherrer Institut Experiment R-99-07, *A Precision Measurement of the Positive Muon Lifetime using a Pulsed Muon Beam and the μ Lan Detector*.
- [63] Paul Scherrer Institut Experiment R-97-05, *Precision Measurement of Singlet μp Capture in Hydrogen*.
- [64] S. Ritt and P. Amaudruz, "The MIDAS DAQ system," *Proc. of the 10th IEEE Real Time Conference*, pp. 309-312, <http://midas.psi.ch>.
- [65] BTRAF J. Sandweiss et al., BNL Bubble Chamber Group Report H-11 (1962), with additions by H. N. Brown (1982) and A. S. Carroll (1983).
- [66] This section was adapted from Yuri F. Orlov and Yannis K. Semertzidis, Muon ($g - 2$) Note

431, January 21, 2003.

- [67] This section was adapted from a preprint by I.A.Koop, A.V.Otboev, E.A.Perevedentsev, P.Yu.Shatunov and Yu.M.Shatunov of the Budker Institute for Nuclear Physics, Novosibirsk.
- [68] L.D.Landau, E.M.Lifshitz, "Mechanics", Moscow "Nauka" (1988)
- [69] A.N.Dubrovin, "MERMAID user guide", Novosibirsk (1994).
- [70] E.A.Perevedentsev et al., Preprint BINP, Novosibirsk (1980)
- [71] Note, other small uncertainties raise the total to 0.21 ppm; these uncertainties are limits, which scale with the size of the data set and thus are not expected to change our projections significantly.

APPENDIX A: NEW BEAMLIN CONCEPT

The conceptual design of the new beamline has been simulated with **TRANSPORT** and **DECAY TURTLE** Ref. [52]. These programs have the functionality of **BTRAF** Ref. [65], the program with which the original beamline was designed. Fig. 18 is a **TRANSPORT** calculation of the pion beam envelope and dispersion of the E821 beamline. This result is identical to the one shown in Figure 6.3.2 of the E821 Design Report. The beamline is comprised of five sections: the pion collection and pion spectrometer section, the matching section, the decay channel, the muon spectrometer, and the matching section to the storage ring. A dispersed focus is produced by the Q1Q2D1D2Q3Q4 at the slits K1K2, and the dispersion is removed by Q5Q6D3D4. Q7 through Q10 rotate the beam envelope of both planes to produce a double waist at the center of Q11. Q11 through Q19 are a simple FODO channel with a phase advance per cell of 90° . D5Q20Q21Q22 produce a dispersive focus at the slits K3K4 just upstream of Q23, and Q23Q24Q25D6 remove the dispersion. Finally, Q26Q27Q28Q29 reform the beam envelope for passage through the inflector and then into the storage ring. These optical constraints determine an essentially unique tune for the beamline. The measured beam profiles in E821 were in very good agreement with the **BTRAF** simulation.

The inflector represents the limiting aperture of the beamline. Q26Q27Q28Q29 must be used to maximize the stored muon beam and not simply be used to maximize the transmitted flux through the inflector. Since no change in the physical aperture of the inflector is under consideration, in all simulations of the new beamline the tune of Q26Q27Q28Q29 has not been changed from the operating point of E821. The working hypothesis is then that if Q26Q27Q28Q29 are not unchanged in the calculation, then a comparison between the calculated flux through the inflector in a modified beamline to the calculated flux through the inflector in the E821 beamline represents a valid estimate of the effectiveness of the modification. A more detailed studied would include the simulation of muon storage after passage through the inflector.

a. Quad Doubling

Increasing the number of quadrupoles in the decay channel is one possible modification of the beamline. The decay channel contains the pion flux. Muons from pion decay are emitted

along the decay channel isotropically in the pion rest frame. The laboratory momentum and angle are governed by two-body decay kinematics and the initial pion momentum and angle. Only muons in a narrow momentum band near the magic momentum of 3.094 GeV/ c are stored by the ring. In addition, the muons must remain within the admittance of the channel and storage ring. The maximum number of stored muons is obtained when the mean decay angle is 0° , and the pion momentum is 0.5% greater than the magic momentum. The momentum difference between the pions and muons is, however, too small to be separated in the muon spectrometer. In E821, to allow effective separation of the pions and muons, the pion momentum was 1.7% above the magic momentum. The mean decay angle in the laboratory is approximately 4 mrad, and muons produced by pions far from the axis of the channel are lost. Fewer muons would be lost if the pion beam envelope were smaller. For a given emittance, the maximum extent of the beam envelope x_{max} is proportional to the square root of the maximum of the beta function of the channel, β_{max} . For a FODO lattice, β_{max} is proportional to the length of the FODO cell having a fixed ratio of focal length f to cell length L . The ratio f/L determines the phase advance per cell, μ . Thus if the length of the cell were reduced by a factor of two and μ is not changed, β_{max} is also reduced by a factor of two, and x_{max} is reduced by a factor of $\sqrt{2}$. Since this reduction occurs in both transverse planes, the increase in transmitted flux could be as large as a factor of two.

The decay channel is comprised of nine quadrupoles that form four cells. With 17 quadrupoles, eight cells are formed and the phase advance is still a multiple of 360° . Fig. 19 shows the TRANSPORT beam envelope when the number of quadrupoles in the decay channel is doubled. The pion momentum and emittance of the beam is the same as in Fig. 18. The beam envelope in the channel is smaller. In this simulation the effective length of the quadrupoles is unchanged, the length of the cell is smaller by a factor of two, and the magnetic field of the quadrupole, calculated using the standard thick lens transport matrix, increases from 1.788 kG to 3.671 kG. The transmission through the lattice was simulated with DECAY TURTLE. For the same beam emittance, apertures, and slit settings, the number of muons passing through slits K3K4 increases by a factor of 1.97, and the number of muons exiting the inflector increases by a factor of 2.61. Thus the expectation of a factor of two increase is verified. Since the calculation does not simulate capture by the storage ring, the increase above the factor of two needs further examination. Increasing the number of quadrupoles in the decay channel does increase the muon flux; however, the pion

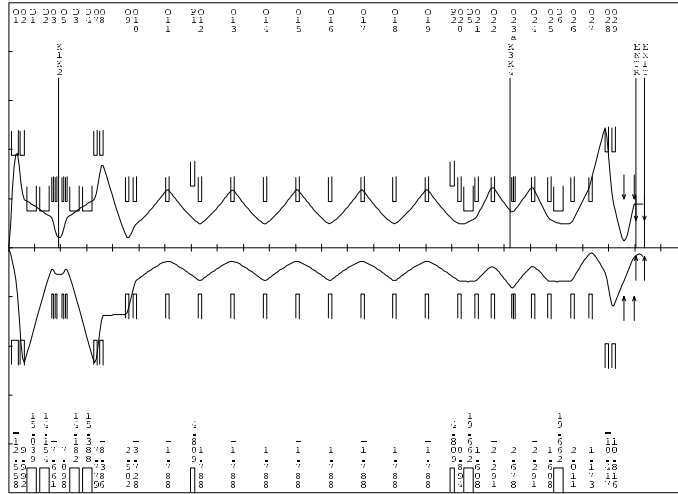


FIG. 18: TRANSPORT calculation of the beam envelope and dispersion of E821 beamline for muon injection tune. The results of this calculation are very similar to the calculation shown in the E821 Design Report. The top panel represents the vertical envelope of the beam; the bottom is the horizontal envelope.

contamination remains.

b. Backward Decay Beam

Highly polarized muons can also be produced by backward decays in the pion rest frame. Pions of $5.324 \text{ GeV}/c$ produce muons of the magic momentum in the backward decay, and magic momentum muons could easily be separated from the higher momentum pions. Modifications of the E821 beamline to use backward decays are considerably more extensive than the modifications required of the decay channel. The beamline must transport $5.324 \text{ GeV}/c$ pions to the end of the decay channel. Simultaneously, it must transport $3.094 \text{ GeV}/c$ muons produced in the decay channel. The rigidity of the pions is larger by a factor of 1.689. With this increase in rigidity and with no change of the bend angles the required fields in D1 through D4 are 25 kG. These fields are large, but they may be possible with limited dipole apertures. With no change in the optics of the pion capture section, the field required in

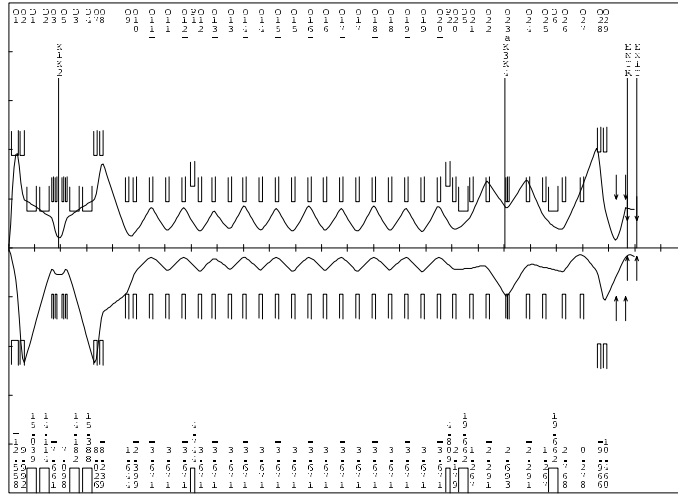


FIG. 19: TRANSPORT calculation of the beam envelope when the number of quadrupoles in the decay channel is doubled. The same emittance beam is transported in this calculation as in 18. The maximum size of the beam is reduced.

the first quadrupole exceeds the 15 kG pole tip field limit. If Q1 were used at this field, the pion flux that could be captured would be reduced by a large factor, approximately 75%. Although the conceptual design is not completed, several points have been resolved. It is possible to transmit effectively the 5.3 GeV/c pions and the 3.1 GeV/c muons in the decay channel. With a modest change in the length of Q1, a 25% increase, and a modest change in the distance between Q1 and the target, a 10% increase, approximately 85% of the pion flux can be captured with Q1 at its field limit. Doubling the number of quadrupoles in the decay channel increases the muon flux transmitted by the inflector by a factor of two. The range of pion momentum accepted by K1K2 can be increased by a factor of three from 0.66% to 2% with an accompanying increase in the muon flux. The larger momentum bite increases the size of the beam envelope in some places and requires larger aperture quadrupoles. The relative flux between backward and forward decays needs further simulation.

In a FODO channel the beta function depends on the particle momentum through the focal length of the quadrupoles. Fig. 20 shows β_{max} for both forward and backward momentum pions as a function of quadrupole field for the cell length of the E821 beamline. Both curves

have a shallow minimum. At the operating point of the E821 beamline, a field of 1.788 kG, β_{max} for the two momenta differ by only 5.1%. The phase advance for the 3.094 GeV/ c muons is 90° , and for the 5.324 GeV/ c pions it is 43° . The lower phase advance changes the ratio of β_{max} to β_{min} . This difference is evident in the beam envelope shown in Fig. 21. This tune simply scales Q1-Q6 and D1-D4 by the ratio of 5.342/3.152. With this scaling, Q1 exceeds the 15 kG field limit by 40% (21.2 kG). The fields of Q7 through Q10 and several quadrupole separations have been tuned to rotate the beam ellipse to produce a waist in the center of Q11. The pions are transmitted through the channel with an acceptable beam envelope. Recall that the channel also transmits magic momentum muons with an acceptable beam envelope. The beam envelope after the decay channel should be ignored. This part of the beamline retains the fields appropriate for 3.094 GeV/ c . Fig. 22 shows the beam envelope when the number of quadrupoles in the channel is doubled. Again the beam envelope is acceptable. The DECAY TURTLE simulations of these two beamlines shows that doubling the number of quadrupoles increases the flux transmitted by the inflector by a factor of 2.1. Again a smaller pion beam in the decay channel has the effect of increase the number of captured muons.

If Q1 is set to the 15 kG field limit, no acceptable tune is possible with this beam emittance. The beam is lost in Q2 in the vertical; the focal length of Q1 is too long. The focal length of Q1 can be decreased by an increase in the length of Q1. Fig. 23 shows the beam envelope that can be obtained with a longer Q1. This beam envelope is acceptable. The field limit of Q1 then does not appear to be a crucial factor in the consideration of backward decays.

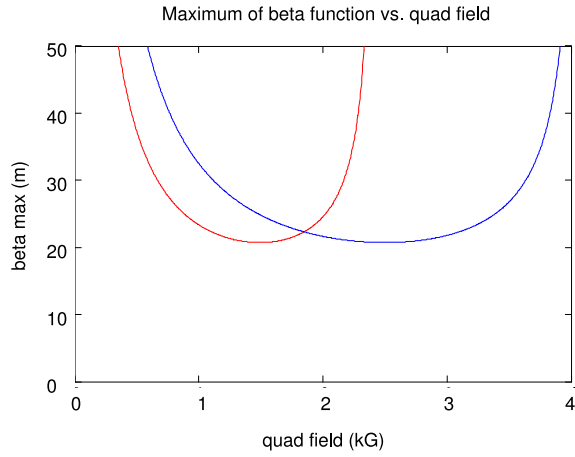


FIG. 20: Calculation of the maximum of the beta function for a simple FODO lattice as a function of the field in the quadrupoles. The cell length is the same as in 19. The two curves are for pions of momenta that produce magic momentum muons by forward and backward decays. The operating point of the channel is at 1.788 kG. At this field, β_{max} for the two momenta are within 5%.

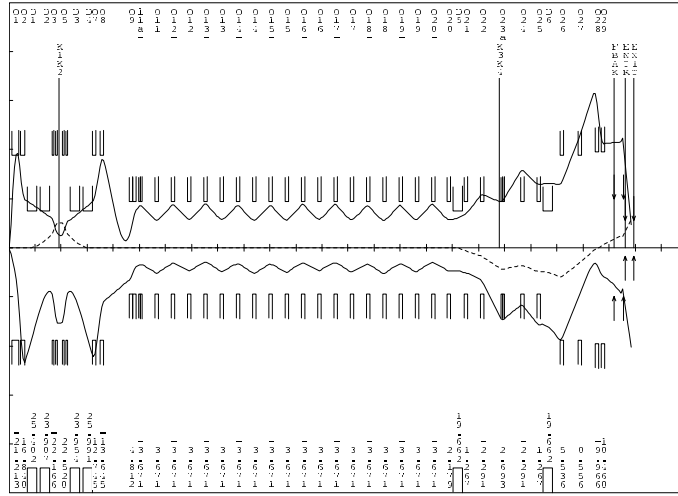


FIG. 22: Similar TRANSPORT calculation to 21 except the number of quadrupoles in the decay channel is doubled. The beam envelope is smaller in the decay channel than in 19.

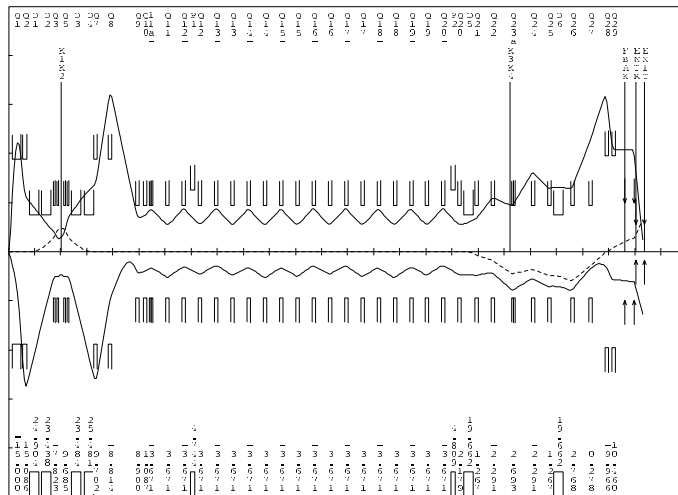


FIG. 23: TRANSPORT calculation that demonstrates that an acceptable beam envelope can be achieved by lengthening Q1 with its field limit.

c. Summary of Design

We have described two major changes to the existing E821 beamline. The increase in stored muon flux that will result is being modelled using the Monte Carlo program `DECAY TURTLE`. The new tunes were optimized using `TRANSPORT`. We find that doubling the quads in the FODO section essentially doubles the muon flux. Tripling or quadrupling the number of quads—there is room—may provide additional flux. A backward decay beam is ideal because it will eliminate the hadron-induced flash. We are beginning to model this beam and have been successful in developing a tune that can transport up to 2 times more pions through the end of the FODO section. The beamline then remains the same as it is presently, optimized to transport magic-momentum muons into the storage ring. Muons created from the backward decay of the 5.3 GeV/ c pions fill a different phase space compared to those for which our forward decay channel has been optimized to transport. We are presently developing a tune to efficiently transport these muons into the storage ring. At this time, we cannot be quantitative on the expected flux. We assume no significant gain or loss in our rate calculations. At the current level of our understanding, a “safe” factor of 2 can be assumed from the quad doubling and an additional factor of 2 from the inflector replacement. Additional gains await more complete beam transport studies.

The hardware implications have been mentioned in the main body of this proposal but include at least a doubling of the FODO quads, modifying the front-end dipoles, lengthening Q1, and moving the production target (within the blockhouse). Several quads in the upstream portion of the beam must be replaced with those having slightly larger apertures.

APPENDIX B: BEAM DYNAMICS AND SCRAPING

1. The Kicker and Quadrupoles

The incoming bunched beam from the AGS is kicked on orbit by a fast muon kicker consisting of three identical pulse-forming networks and kicker magnets.[13] The fast muon kicker worked adequately during the running period of E821, but there are several maintenance items which must be attended to. The first kicker unit must be repaired to replace a cracked ceramic insulator, which prevented it from holding full voltage. We are also studying the absolute injection efficiency to see if an additional kicker module might improve the reliability and efficiency of injection. The rate calculations in this proposal do not assume any additional factor from the kicker.

The electrostatic quadrupoles, which provide the (weak) vertical focusing in the storage ring, worked well in E821. We do need to improve the lead geometry inside of the vacuum chamber to further reduce trapped electrons, as well as improve the lead configuration outside of the vacuum chamber where the high voltage feed-throughs are located to make them more reliable. These changes represent modest improvements and will not be discussed further in this proposal.

2. Beam Dynamics in the Ring

The storage ring is a weak focusing ring, with the field index $n < 1.0$ determined by the strength of the electrostatic quadrupole field. In the limit of a continuous quadrupole field, the stored muons execute simple harmonic motion radially (x) and vertically (y) with the frequencies given by

$$f_y = f_C \sqrt{n} \simeq 0.37 f_C; \quad f_x = f_C \sqrt{1-n} \simeq 0.929 f_C, \quad (\text{B1})$$

where f_C is the cyclotron frequency. The numerical values are for $n = 0.137$. The frequencies in the ring are given in Table VI.

One of the systematic errors which must be improved in the new experiment comes from muon losses out of the storage ring which result from processes other than muon decay. In E821 we reduced these losses by scraping off particles on the edge of the storage volume. Scraping is defined as the creation of a gap of several mm between the beam

<i>Quantity</i>	<i>Expression</i>	<i>Frequency</i>	<i>Period</i>
f_a	$\frac{e}{2\pi mc} a_\mu B$	0.23 MHz	4.37 μs
f_c	$\frac{v}{2\pi R_0}$	6.7 MHz	149 ns
f_x	$\sqrt{1-n} f_c$	6.23 MHz	160 ns
f_y	$\sqrt{n} f_c$	2.48 MHz	402 ns
f_{CBO}	$f_c - f_x$	0.477 MHz	2.10 μs
f_{VW}	$f_c - 2f_y$	1.74 MHz	0.574 μs

TABLE VI: Frequencies in the $(g - 2)$ ring. *CBO* = coherent betatron oscillation; *VW* =vertical waist; a, c refer to spin precession ω_a and cyclotron frequencies respectively.

and the collimators that will either eliminate altogether or drastically reduce particle losses during data collection time. This was achieved by asymmetrically powering the electrostatic quadrupoles during and after injection for 10-15 μs and scraping the beam on collimators placed around the ring. This asymmetry caused the beam to be lifted and moved sideways during this scraping time. At the end of the scraping period, the beam was returned to the equilibrium orbit with a 5 μs time constant. While losses were reduced from 0.6% per muon lifetime in the ring with no scraping to 0.2% with scraping, we will need to do better in the new experiment.

Because of the small inflector size relative to the storage volume, shown in Fig. 24, the phase space in the ring is not uniformly filled. This causes the bunched beam to oscillate coherently both vertically and horizontally in the storage ring. For a detector at a fixed point in azimuth, the apparent radial motion of the beam is the difference frequency between the cyclotron frequency and the horizontal betatron frequency given in Eq. B1. The inflector image is re-formed every betatron wavelength, so that this “waist” in the beam also moves around the ring with the difference frequency between the the cyclotron frequency and twice the radial (vertical) betatron frequency. Since the detector acceptance depends on the radial position of the muon when it decays, the coherent radial betatron oscillations (CBO) amplitude-modulate the time spectrum. The modulation effect decreases in the time due to the “natural” chromaticity of the betatron oscillations, which slightly mix up phases of the particle oscillations. In E821 we measured a decoherence time of about 100 μs for the CBO,

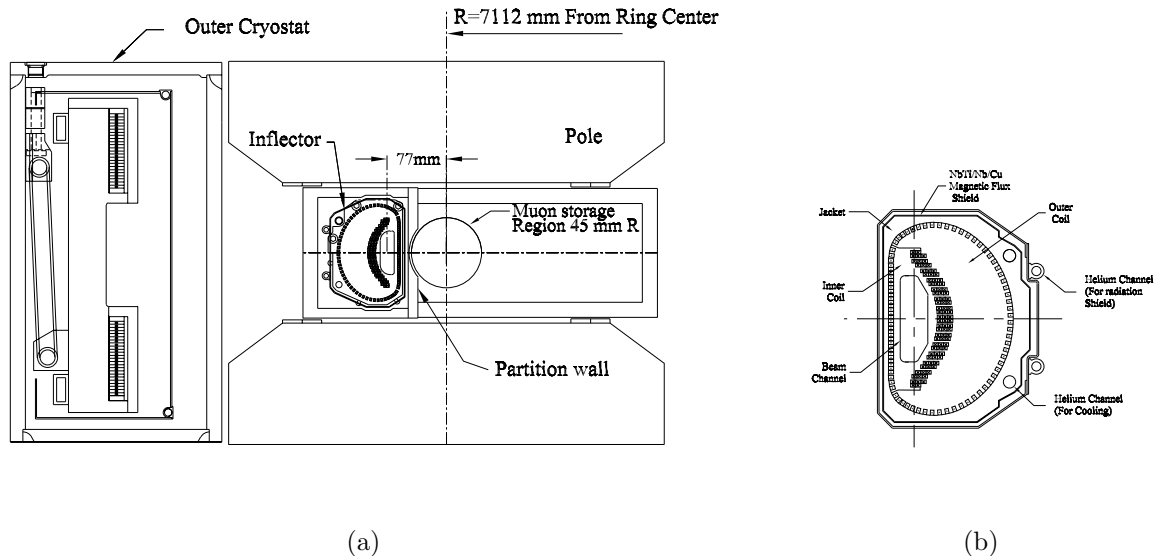


FIG. 24: (a) The geometry of the inflector exit and the muon storage volume. (b) The cross section of the inflector.

and the muon lifetime was $64.4 \mu s$.

In the new experiment we wish to reduce the CBO effects, and to improve the scraping of the beam. Two approaches to reduce the coherent betatron motion and scrape the beam have been proposed:

1. Using a RF dipole field during the time immediately after injection to first drive the coherent betatron oscillations to scrape the beam, and then to reverse the phase to damp the CBO. This technique would get rid of the main CBO but not the “waist” motion in the beam.
2. A scheme which causes a fast phase mixing in the betatron tune through the introduction into the machine lattice of a nonlinear focusing element such as an octupole. Preliminary studies indicate that the CBO modulation can be minimized by applying this field during less than a hundred turns after injection. This will also serve the purpose of scraping the beam simultaneously with the CBO decoherence.

3. Oscillating Dipole Method of Scraping[66]

In E821 we have estimated the horizontal CBO amplitude at injection both directly and indirectly. The first method involved the fiber beam monitors (see Fig. 25) which consist of eight 0.5 mm diameter scintillating fibers which are inserted into the beam to measure the profile. The signal from a single vertical and single horizontal fiber are shown in Fig. 26 where the beam motion across the fiber is clearly seen. The measured CBO amplitude was found to $\simeq 7$ mm with a frequency $\omega_{CBO} = \omega_C(1 - \sqrt{1 - n}) \simeq 470$ KHz.

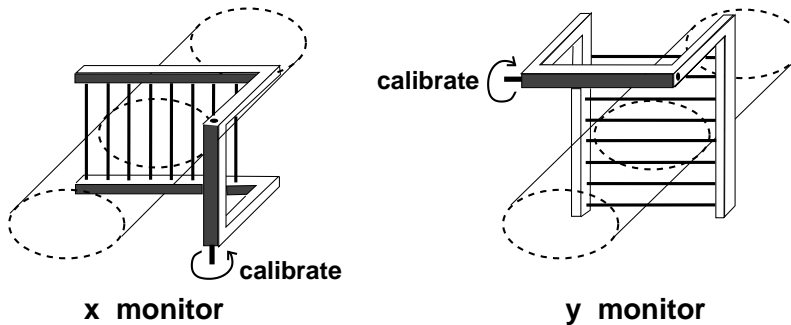


FIG. 25: A sketch of the x and y fiber beam monitors. The fibers are 0.5 mm in diameter. For calibration, the entire “harp” rotates into the beam so that all fibers see the same beam intensity.

This beam CBO manifested itself, among other ways, as a modulation of the number of detected positron by the electromagnetic calorimeters with an amplitude of $\simeq 1\%$. Monte Carlo studies showed that an amplitude of $\simeq 7$ mm for the CBO would cause that modulation amplitude. Vertically the CBO amplitude is much smaller but still visible from the data at early times. With similar beam injection conditions the CBO has a well defined frequency, amplitude and phase. We propose to use this fact to both scrape the beam and eliminate the horizontal and vertical CBO of the beam due to the motion of the beam center.

This proposal uses a set of four plates, with $l = 1$ m long azimuthally and placed in the configuration of the quadrupole plates in the g-2 ring. We will then apply a voltage difference between the opposite plates with a frequency equal to the horizontal (horizontal plates) and vertical (vertical plates) CBO. For scraping the beam we will apply the voltage in phase with the beam CBO phase to increase the CBO amplitude. To eliminate the CBO the phase will be opposite. To estimate the voltage needed we will consider here the horizontal CBO, but the same method can be applied for the vertical CBO. The functional form of the

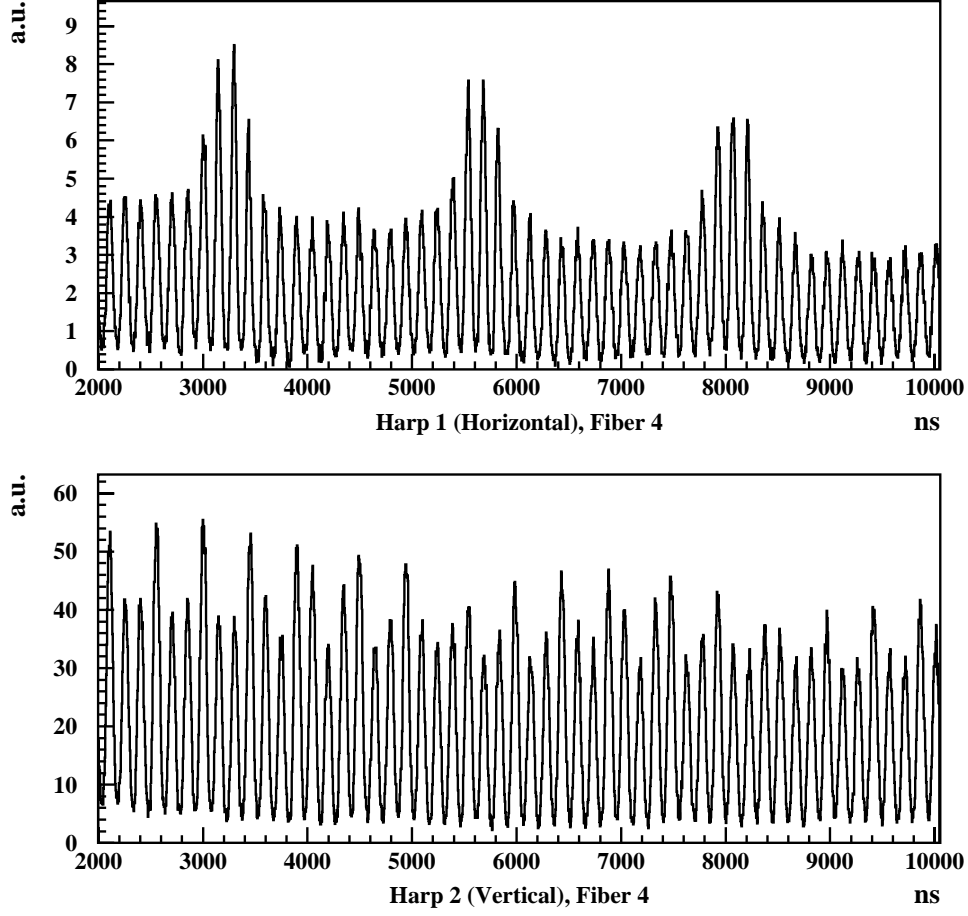


FIG. 26: The phototube output from a single x and y fiber. The CBO frequency (horizontal) and VW frequency (vertical) are clearly seen (see Table VI).

horizontal dipole electric field, $E_x(t)$, is

$$E_x(t) = E_{x0} f(s) \cos(\omega_{CBO}t + \theta_0), \quad (\text{B2})$$

where $f(s) = 1$ for the space between the plates and 0 outside them. We take as $t = 0$ the time the muon beams enter the electric plates for the first time. Then the equation of motion can be written as

$$\ddot{x} + \omega_C(1 - n)x = \omega_C^2 R \left(\frac{eE_{x0}}{\beta B} \right) f(t) \cos(\omega_C(1 - \sqrt{1 - nt} + \theta_0)) \quad (\text{B3})$$

where $\beta \equiv v/c$ and

$$f(t) = \begin{cases} 1, & Tq < t < (Tq + \frac{l}{v}), \quad q = 0, 1, \dots, N \\ 0, & \text{otherwise} \end{cases} \quad (\text{B4})$$

Where $T \simeq 149$ ns, the cyclotron period of the ring. The exact solution of equation 3 with $f(t)$ given by Eq. B4 is

$$x = a(t)e^{i\omega_x t} + a^*(t)e^{-i\omega_x t} \quad (\text{B5})$$

$$a = a_0 - ie^{i\theta_0} \frac{N+1}{4\sqrt{1-n}} \left(\frac{E_{x0}l}{\beta B} \right) \left[1 + \frac{e^{i2\theta_0}[1 - e^{-i2\omega_C(1-\sqrt{1-n}T(N+1))}]}{N+1[1 - e^{-i2\omega_C(1-\sqrt{1-n}T)}]} \right]. \quad (\text{B6})$$

where $a_0 = (x_{max}/2)e^{i\alpha}$ corresponds to $t = 0$ and defines the electric field phase θ_0 . After $N + 1$ turns we get Eq. B6 which for large $N > 10$ simplifies to

$$a = a_0 - ie^{i\theta_0} \frac{N+1}{4\sqrt{1-n}} \left(\frac{E_{x0}l}{\beta B} \right), \quad (\text{B7})$$

where B is the storage ring dipole magnetic field. For $x_{max} = 0.7$ mm, $N = 60$ (i.e. about $10 \mu\text{s}$), $n = 0.142$, and $B = 1.45$ T we need $E_{x0} \simeq 0.9$ kV/cm at the CBO frequency of $\simeq 470$ KHz. For a plate separation of 10 cm it means a voltage amplitude of $\simeq 9$ KV across the opposite plates horizontally driven at 470KHz, which is quite reasonable.

The expected beam losses after scraping the beam are going to be dominated by the vertical scraping since it is expected that horizontally we wouldn't need to scrape more than $\simeq 7$ mm oscillation of the beam at injection. Horizontally we would therefore just wait of the order of $5 \mu\text{s}$ for the beam to scrape off the collimators after which we would apply the voltage estimated above to eliminate it. Vertically we would need to apply a voltage for about $5 \mu\text{s}$ after injection in phase with the natural one so that we induce an overall vertical oscillation of the order of 5 mm after which we will flip the sign of the phase to eliminate it. The total beam losses induced by this method of scraping for a beam gap of 5 mm vertically and 7 mm horizontally are estimated to be less than 20%.

4. Pulsed Octupole Method to Remove the CBO[67]

This method effects a fast phase mixing by an introduction of a nonlinear focusing element in the machine lattice. The nonlinearity induces a dependence of betatron tunes on amplitudes of transverse oscillations $(\frac{\delta Q}{\delta a^2})$. [68] The CBO modulation could be minimized during a few tens of turns in the storage ring. Using a time (up to 100 turns) to apply a pulsed closed orbit distortion can make the CBO vanish while simultaneously scraping the beam.

The rectangular symmetry of the vacuum chamber permits one to install an octupole coil inside the vacuum chamber. The coil can be wound around an area of 6 cm radius as shown in Fig. 27, while the beam has $r = 4.5$ cm. In a preliminary design, a coil length of 2 m was chosen, located in a section free from electrostatic focusing and kickers. The field lines have been calculated by the computer code MERMAID.[69]

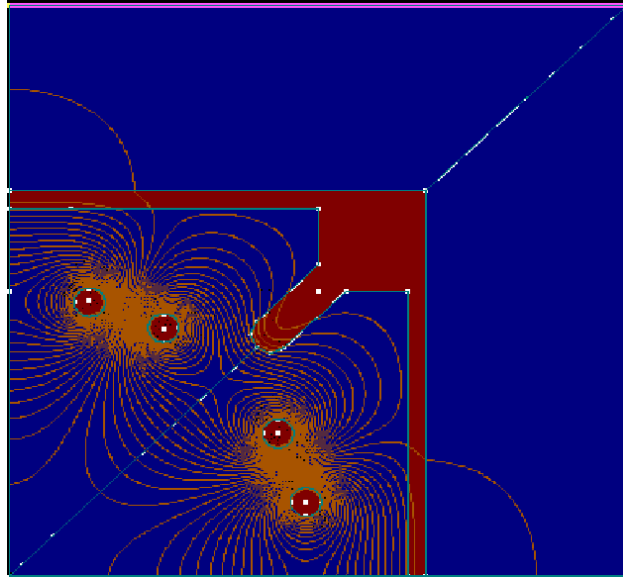


FIG. 27: Octupole coil in vacuum chamber and magnetic field lines

Particle tracking was done with electrostatic focusing of the $(g - 2)$ ring for different octupole field strengths, and for several residual horizontal angles after the kicker. The RING code was used for the tracking,[70] for 10000 particles. The initial phase-space distributions were assumed to be uniform in both the vertical and radial directions. The muons were tracked for 100 turns. The initial and stored phase space distributions are shown in Figs. 28.

During tracking, the amplitude of the CBO was evaluated after each turn by the expression:

$$A = \sqrt{\frac{(1 + \alpha_x^2)\langle x \rangle^2 + 2\alpha_x\beta_x\langle x \rangle\langle x' \rangle + \beta_x^2\langle x' \rangle^2}{\beta_x} + \frac{(1 + \alpha_y^2)\langle y \rangle^2 + 2\alpha_y\beta_y\langle y \rangle\langle y' \rangle + \beta_y^2\langle y' \rangle^2}{\beta_y}}, \quad (\text{B8})$$

where $\langle x \rangle\langle x' \rangle$, $\langle x \rangle^2$, $\langle x' \rangle^2$, $\langle x \rangle\langle x' \rangle$, $\langle x \rangle^2$ are average over the ensemble coordinates and angles and their squared values. α and β — are corresponding Twiss parameters.

Fig. 29 shows the CBO amplitude versus turn number N , for different octupole strengths. One can see an octupole gradient of 0.8 G/cm^2 greatly reduces CBO amplitude by the 30-th

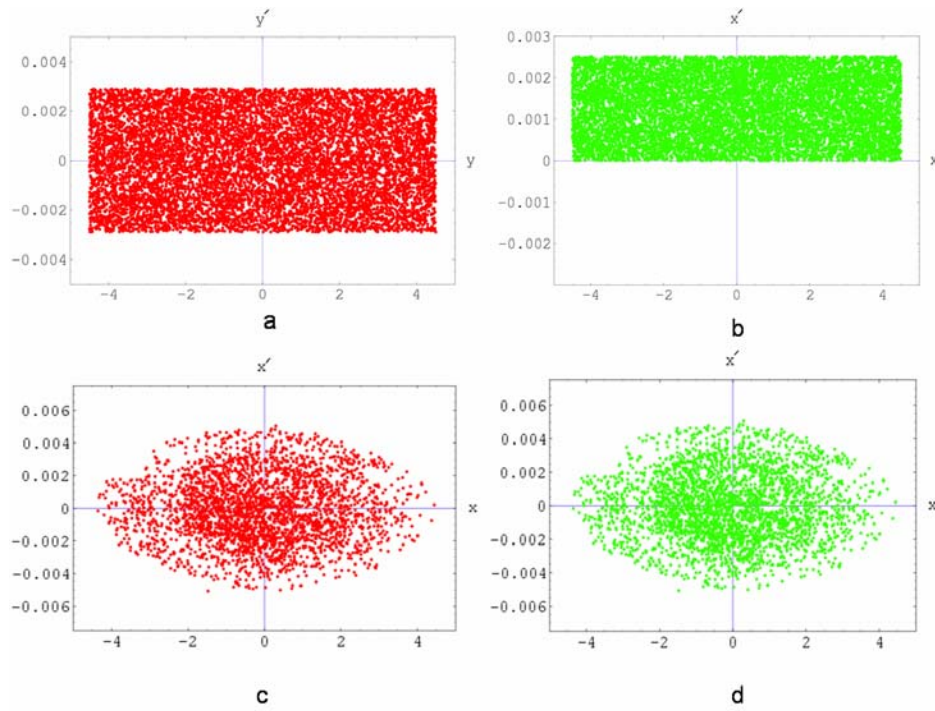


FIG. 28: Initial and final phase distributions. (a) Initial vertical distribution. (b) Initial radial distribution. (c) Stored radial distribution. (d) Stored radial distribution.

turn. The tracking shows that neither this reduction factor, nor the amplitude beating after the octupole is removed, depend on the residual angle. About 50% of the beam is lost using this method.

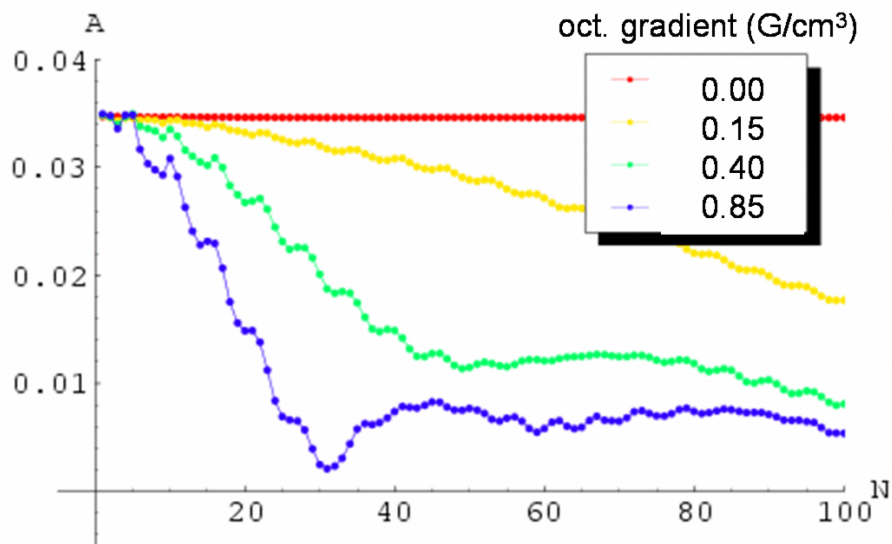


FIG. 29: Behavior of the CBO amplitude as a function of turn number and octupole strength.

Calculations show that to provide the optimal octupole gradient of 0.8 G/cm^2 , a pulse current of 2.5 kA is needed. This will need to be a pulsed octupole, since the octupole field, as well as any magnetic fields induced by eddy currents in the vacuum chamber or other conductors nearby, must be negligible before data collection can begin. Simulations used both a square (ideal) current pulse and a sinusoidal one, and little difference was found compared to the rectangular one. The parameters of an LCR pulse generator are, Voltage $V=1.3 \text{ kV}$, Capacitance $C \approx 1 \mu F$, Period $T \approx 10 \mu \text{sec}$. The octupole coil can be made from water-cooled copper pipe of 1 cm in diameter. The energy dissipated in such a coil per pulse is about 1 J .

An alternative electrostatic octupole is able to do the same, but its realization looks from practical point of view much more difficult, because of the symmetry imposed by the trolley rails which go all the way around inside the vacuum chamber with four-fold symmetry.

APPENDIX C: THE SUPERCONDUCTING INFLECTOR

There are two possible improvements to the superconducting inflector: (i) open the ends, (ii) open up the size of the beam channel. In this appendix we describe the inflector and discuss these options.

In order to inject into the storage ring, it is necessary to bring the beam through a rather large fringe field to the edge of the precision 1.5 T magnetic field. A separate magnet, called the inflector magnet, is needed to cancel this fringe field in order to permit the beam to enter undeflected. The injection geometry is shown in Fig. 30. The beam exiting the inflector is 77 mm from the storage ring center, as is shown in Fig. 31

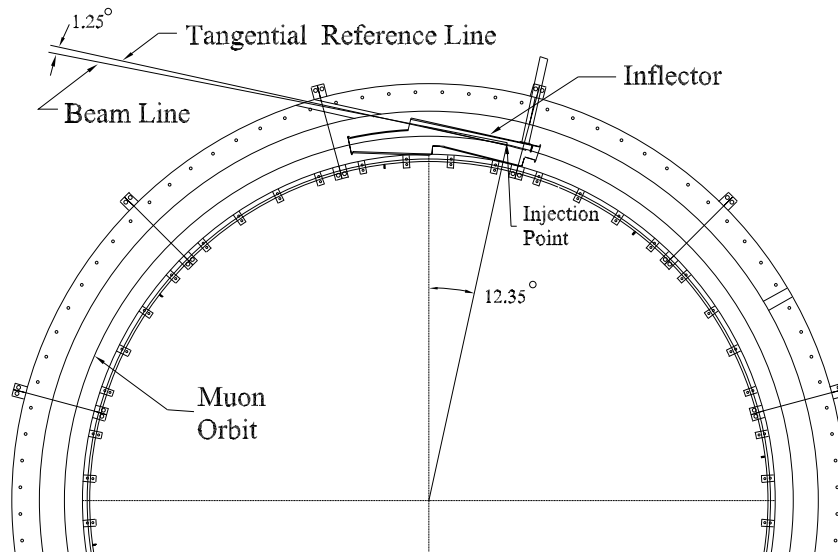


FIG. 30: A plan view of the storage ring and injection line, showing the location of the superconducting inflector.

In the CERN experiment[21], a pulsed co-axial device was employed for this purpose. In E821 it was realized early on that such a pulsed device with the needed repetition rate would be almost impossible to fabricate. Furthermore, the transient effects from such a device could potentially spoil the uniform field seen by the stored muons, and thus introduce serious systematic errors.

The idea of a static superconducting inflector[10] solved these problems, providing that the field leakage from the inflector magnet could be kept out of the storage ring. This was done using a passive superconducting shield[11] which traps any stray flux before it

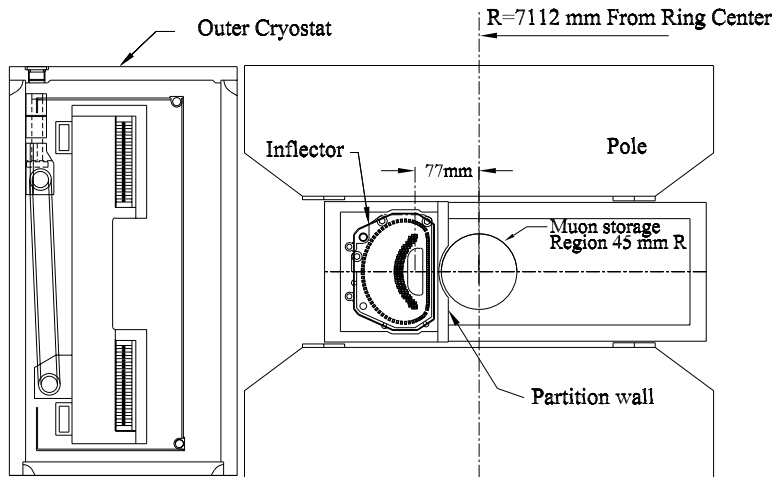


FIG. 31: An elevation view of the inflector exit, the magnet pole pieces, and the beam vacuum chamber.

gets to the storage volume. This idea worked, giving the precision field shown in Fig. 1. Measurements showed that the superconducting sheet holds off up to 1 kG of field. This shielding factor gives a factor of five margin over the measured leakage from the open end prototype.

The inflector is based on a truncated double-cosine theta design, shown in Fig. 32, where the conductors inside of the “D” carries current in the opposite direction from those in the shape of a “D”. The flux configuration, along with the cross section, are shown in Fig. 32. When placed in the fringe field of the magnet, the field is (essentially) zero in the beam channel and 3 T in the return part of the inflector. To reduce the flux density at the superconductor, the area (hence volume) for the return path of the magnetic circuit is much larger than in the beam channel region, which can be seen clearly in Fig. 32. The superconductor in the inner coil has to have a critical current adequate to support the 3 T field without quenching.

In the inflector used in E821, the superconductor was wound over the beam channel so that both ends of the inflector were covered with material. The cable is composed of NbTi:Cu:Al = 1:0.9:3.7, which is equivalent to at total of ~ 13 mm of Al covering the entrance and exit of the inflector beam channel. It is possible to increase the amount of beam stored by opening the inflector ends. Beam transport studies showed a loss in stored

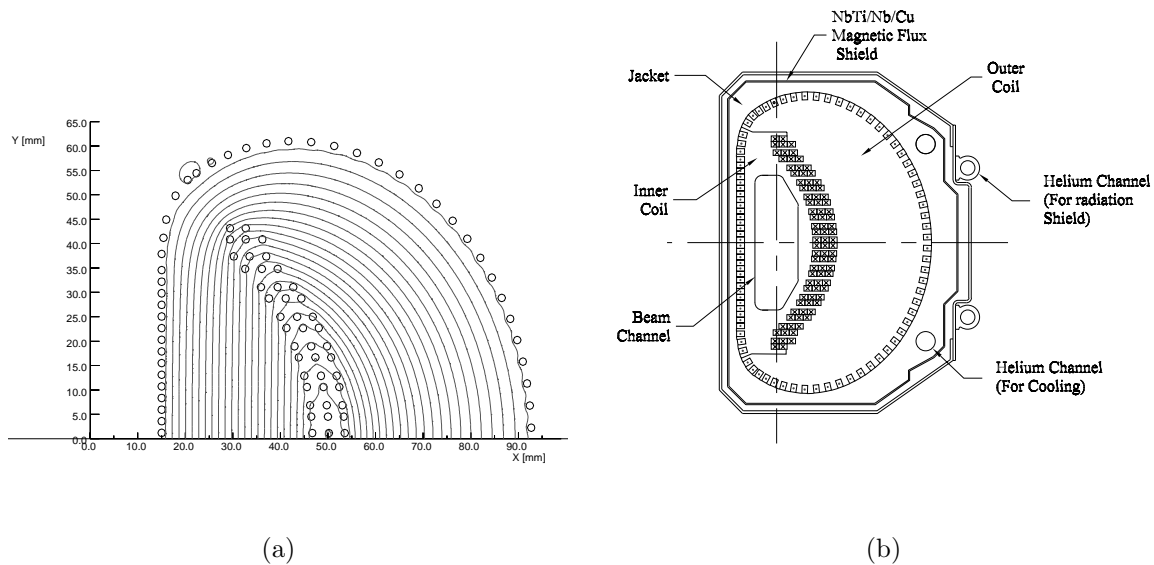
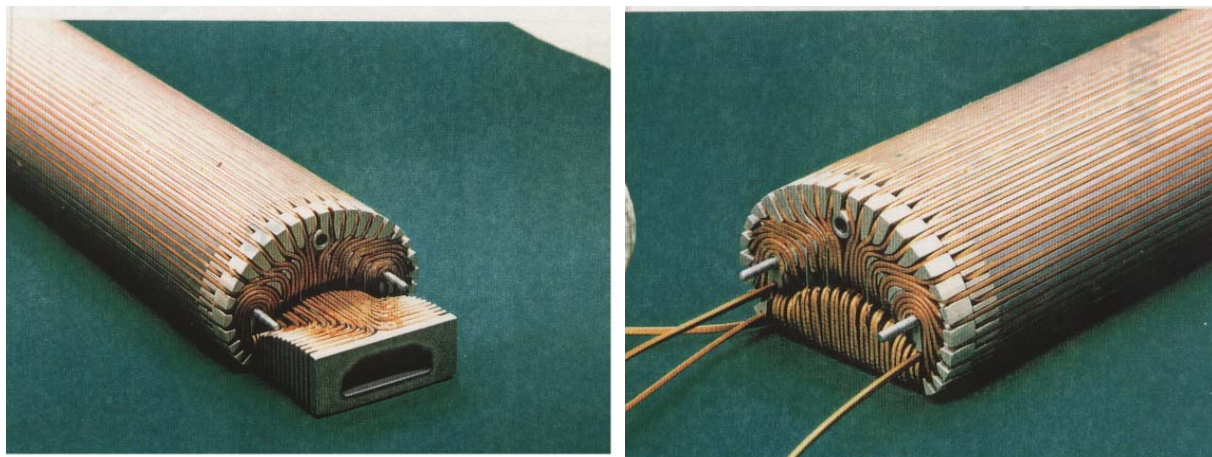


FIG. 32: (a) The conceptual design of the inflector showing the flux path for the upper half. The current in the conductors forming a “D” flows in the opposite direction, from that in the backwards “C”. The geometry is such that there is minimal flux leakage along the body of the inflector. (b) The cross section of the inflector.



(a) Open End

(b) Closed End

FIG. 33: Photos of the open- and closed-end inflector prototype.

muons from multiple scattering and energy loss by a factor of 1.7 (neglecting the Landau

tail) compared to the open-end version. This factor increases to 2 when this tail is included.

While the open end was more complicated to fabricate, during the E821 R&D phase a 0.5 m prototype was built and tested both alone and in an external 1.5 T field.

Nevertheless, we chose the closed end design for E821 since we felt this was a more conservative design, and the muon transmission through it was thought to be adequate to reach our design goal of 0.35 ppm relative error. Our concerns at that time were two-fold: (i) minimizing the stray field at the end of the inflector, and (ii) stability against quenches. Now that we have experience with the passive superconducting shield, we are confident that flux leakage into the storage volume will not be a problem. We will revisit the question of stability, but since the open end prototype worked well in an external field, we are confident that a working inflector can be made with both ends open.

APPENDIX D: NEW CALORIMETERS

The basic material design requirements for a new calorimeter are largely unchanged; it must be dense and fast. Additionally, the new calorimeter must be segmented transversely with respect to the incoming positron, so that simultaneous events can be distinguished 4 out of 5 times. Building new Pb/SciFi calorimeters with fibers running longitudinally (i.e., rotated by 90 degrees) is one possible solution. The downstream face of the detector would be a fiber / lead grid that could be readout in small and independent segments. Members of our Collaboration have built detectors of this type in the past, with incoming photons nearly co-linear with the fiber direction (see Ref. [20]). This re-oriented Pb/SciFi option is attractive in principle, but there are two drawbacks. First, the downstream space is limited by the existing vacuum chamber structures. A denser detector is desired to open up additional space for the readout system. Second, simple simulations using $\rho_M = 2.5$ cm and the requirement that showers be separated by at least $2\rho_M$, indicate a pileup separation factor of no better than 3 (the simulation uses the actual distribution of electrons on the calorimeter face, see Fig. 34). The goal of the new detectors is to separate simultaneous showers by a factor of about 5. To do so requires the detector to have a smaller Moliere radius.

A simple detector, which should satisfy our needs, can be assembled from alternating layers of tungsten (W) and plastic scintillator. The scintillator is envisioned to be made from ribbons of adjacent 0.8 mm diameter single-clad fibers. The W plates are also 0.8 mm thick. Each module is 4×4 cm and has a length of 11 cm ($15X_0$). The fiber ribbons are oriented vertically so that the positrons, which are curling inward, must cross W layers and initiate showers. The individual modules are stacked in a 4×5 array to form a detector that is 16 cm high by 20 cm radially. The increased height compared to the 14 cm high E821 calorimeters improves overall shower containment and reduces sensitivity to vertical width fluctuations induced from the coherent betatron modes. The reduced radial dimension $22.5 \rightarrow 20$ cm accepts fewer low-energy positrons, which are the least interesting as they carry a lower asymmetry.

Figure 35 shows one calorimeter module. A lightguide is made from a tapered section coupled to a laminated acrylic sheet bundle bent at 90 degrees toward the inside of the ring. Lightguide extension rods will pipe the light to an array of 20 PMTs located about 1 m away.

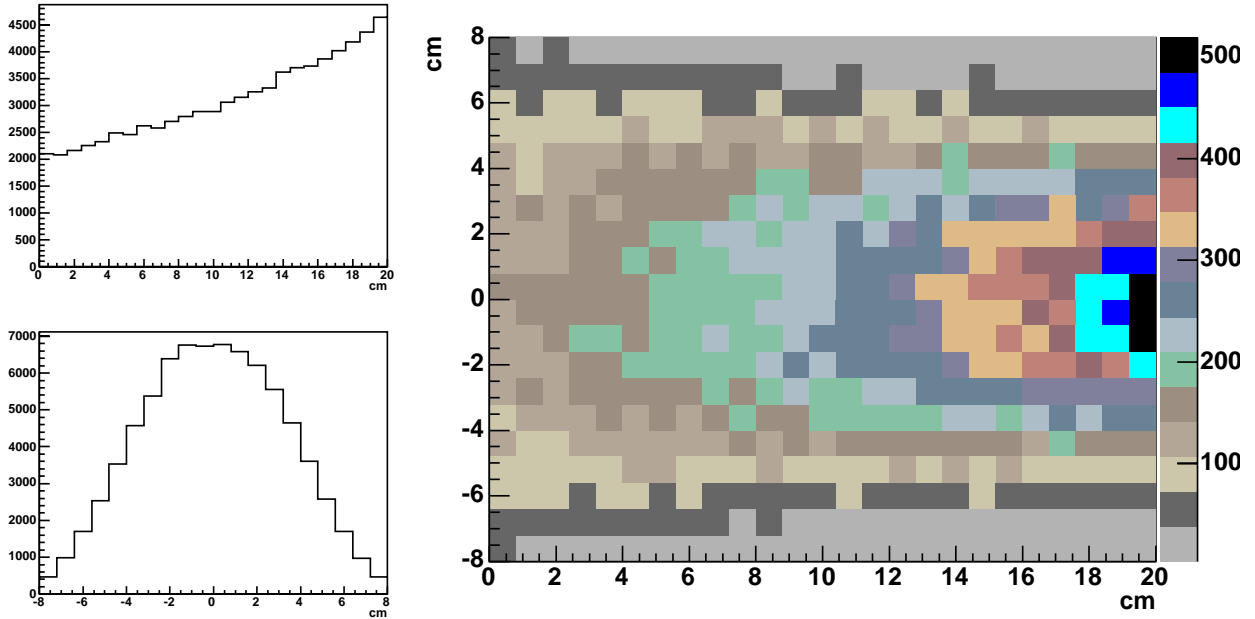


FIG. 34: Right panel: Hit position of positrons on calorimeter front face from from GEANT simulation. Top left panel: radial distribution; storage ring edge is at large x values. Bottom left: vertical distribution.

The distance is required to keep the PMTs sufficiently away from the storage ring magnetic field and to keep the PMT shielding materials sufficiently far away from perturbing field. A complete calorimeter, including lightguides, is shown in Fig. 36. Its assembly position, with respect to the existing scalloped vacuum chamber, is shown in Fig. 37. As is evident, the space is quite tight.

The 29-mm (1-1/8 in) PMTs have not yet been selected but their basic characteristics are understood and standard. We are using an array of 340 Photonis XP-2982, 11-stage PMTs for the muon lifetime experiment MuLan at PSI. The similar 10-stage XP-2972 is more appropriate for P969 because of the high light yield from the calorimeter modules. Both tubes were carefully evaluated by us and feature similar important characteristics: low noise, high gain, no detectable after-pulses. We will have to design a robust, rate-dependent base as the initial rate of up to a few MHz is higher than what can be comfortably handled by the stock resistor divider network in the simplest Photonis bases.

Preliminary GEANT simulations have been performed to evaluate the performance of the W-SciFi calorimeter subjected to the decays from muons in our tracking simulations. The

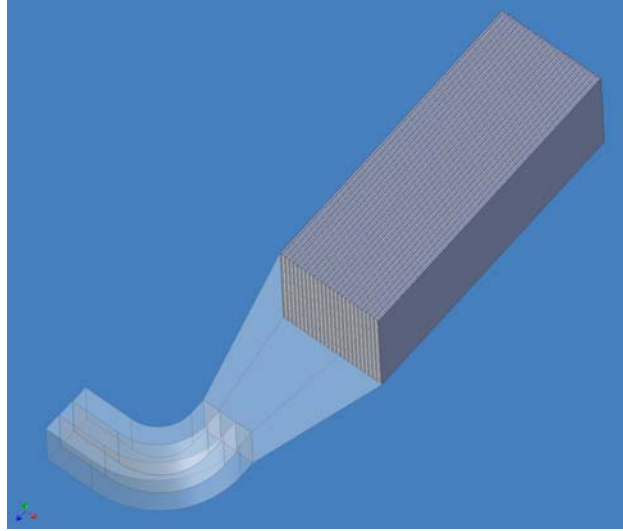


FIG. 35: One of the 20 calorimeter segments. Each segment contains 25 layers having a 0.8 mm tungsten plate and a 25-fiber ribbon of 0.8 mm scintillating fiber. The segment is $4 \times 4 \times 11$ cm. A schematic lightguide includes a tapered section, followed by a laminate of thin sheets of acrylic, bent toward the inside of the storage ring.

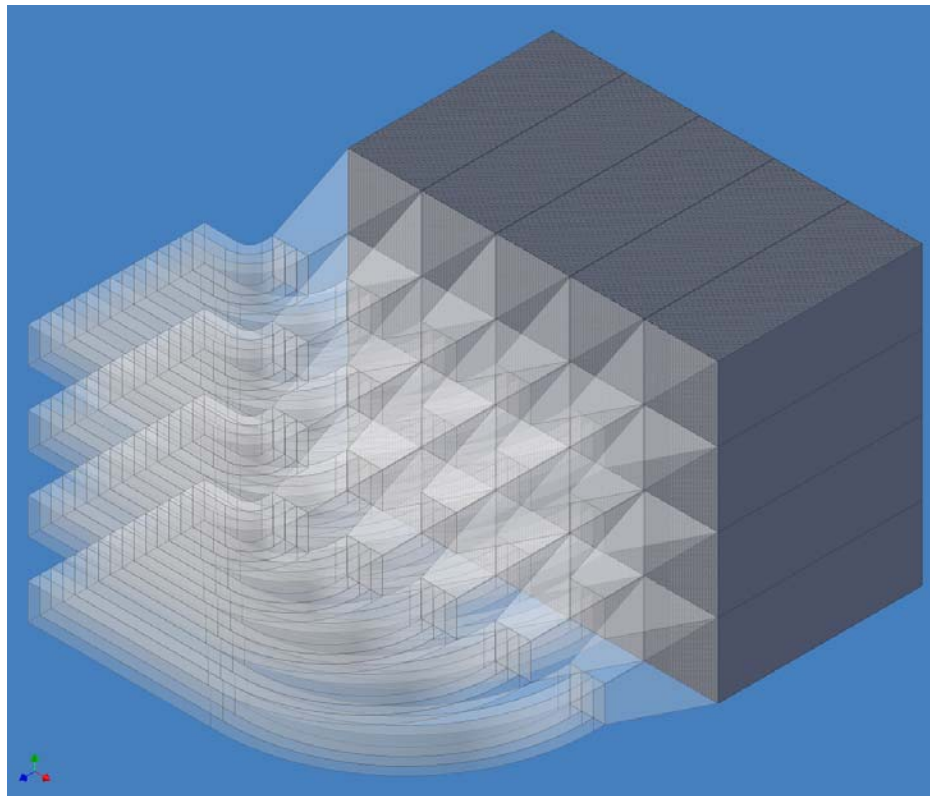


FIG. 36: Schematic of the segmented calorimeter lightguide arrangement.

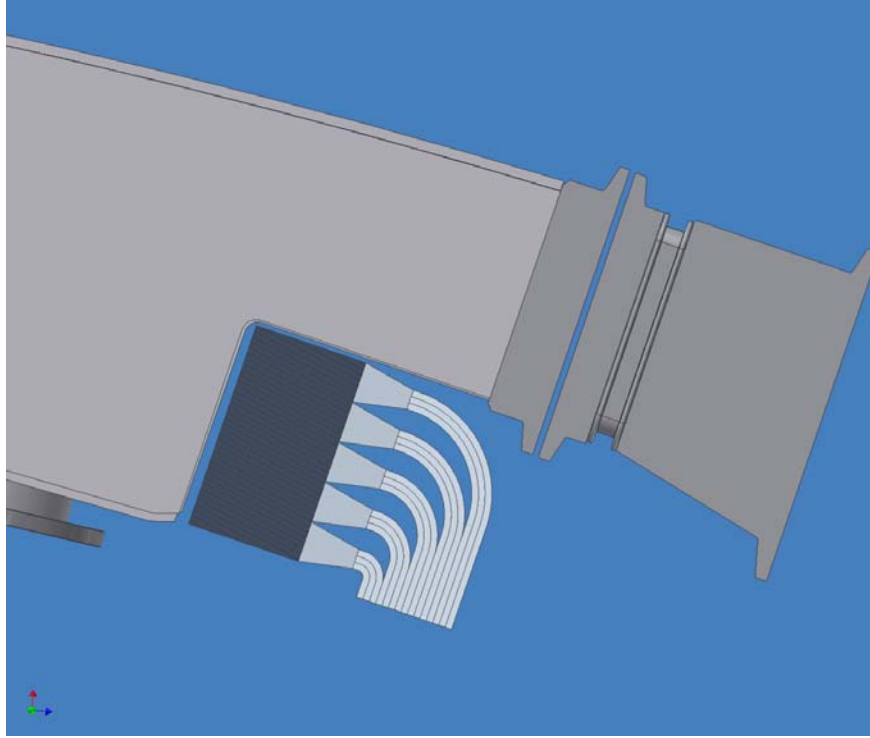


FIG. 37: Plan view of new calorimeter in the region of the bellows between vacuum chambers where the available space for lightguides is quite restricted.

reconstructed resolution in this 50:50 mixture of tungsten and scintillator is approximately

$$\sigma/E = 14\%/\sqrt{E}.$$

A plot is shown in Fig. 38. This resolution can be improved by slight adjustments of the ratio of materials or in the size of layers. The final detector will be optimized for pileup rejection and resolution requirements, the latter being relatively modest for the $(g - 2)$ experiment. The simulations were also used to “measure” the effective Moliere radius, both vertically (where it is expected to follow standard calculations) and horizontally (where it broadens due to impact angle and field orientation). Fig. 39 shows the ratio of energy deposited in one row as a fraction of the total energy as the incoming positron impact position is varied vertically. For all energies, the ratio changes with the same shape. Fig. 40 is similar but instead corresponds to the horizontal (radial) ratio. The positrons are curling to the left in this figure and their impact angle on the calorimeter face is energy dependent; high-energy positrons enter nearly orthogonal, but low-energy positrons can hit the front face with an angle as large as 30 degrees. The broadening, and shifting, of the ratio function is evident

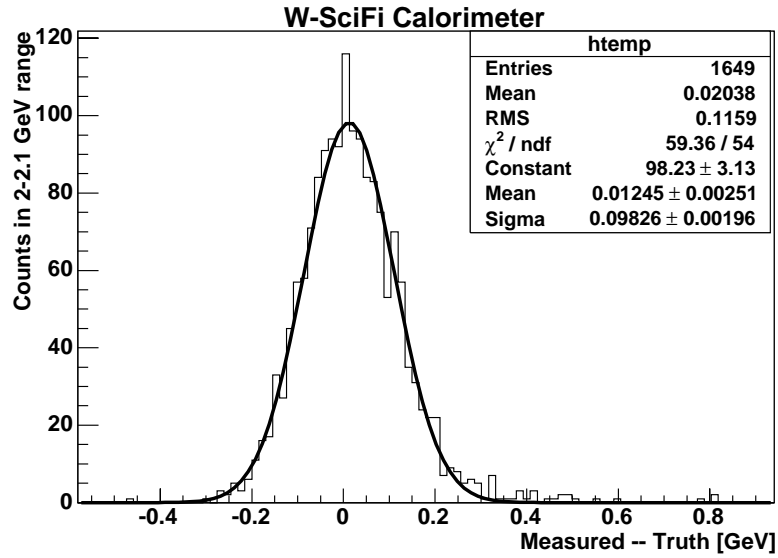


FIG. 38: Reconstructed energy vs. actual energy of positrons from GEANT simulation into W-SciFi sampling calorimeter. A cut is made from 2.0-2.1 GeV; the resolution is approximately 10%.

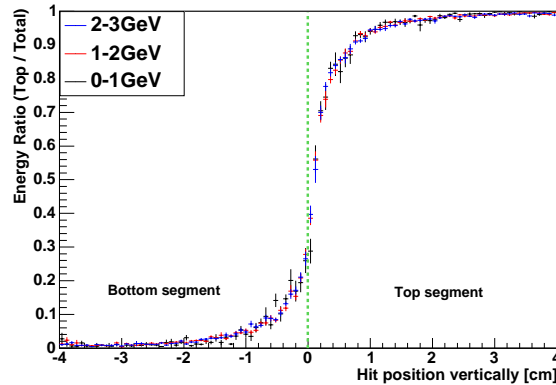


FIG. 39: Ratio of energy deposited in the top rows vs. the total as a function of vertical impact position. The green dashed line represents the boundary in the middle of the calorimeter. The three bands correspond to different positron energies.

in this figure. We are using this detailed simulation to develop algorithms to distinguish simultaneous events having different energies and impact positions.

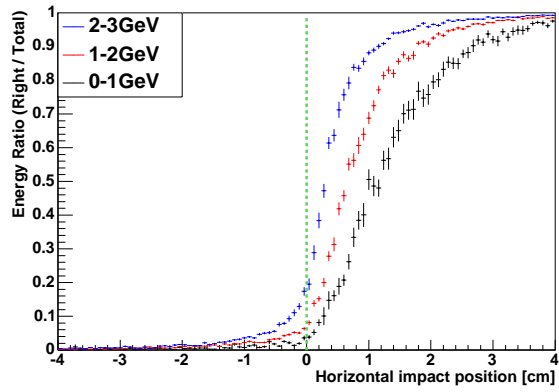


FIG. 40: Ratio of energy deposited in the ‘one side vs. the total as a function of horizontal (radial) impact position. The green dashed line represents the center of the calorimeter. The three bands correspond to different positron energies. Low-energy positrons strike the calorimeter at a non-negligible impact angle, pointing to the left in this figure.